

What dominates the coronal emission spectrum during the cycle of impulsive heating and cooling?

S.J.Bradshaw

Department of Physics and Astronomy, Rice University, Houston, TX 77005, USA

`stephen.bradshaw@rice.edu`

and

J.A.Klimchuk

NASA Goddard Space Flight Center, Solar Physics Lab., Code 671, 8800 Greenbelt Road,
Greenbelt, MD 20771, USA

`james.a.klimchuk@nasa.gov`

Received _____; accepted _____

For submission to the Astrophysical Journal

ABSTRACT

The “smoking gun” of small-scale, impulsive events heating the solar corona is expected to be the presence of a hot (> 5 MK) plasma component. Evidence for this has been scarce, but has gradually begun to accumulate due to recent studies designed to constrain the high temperature part of the emission measure distribution. However, the detected hot component is often weaker than models predict and this is due in part to the common modeling assumption that the ionization balance remains in equilibrium.

The launch of the latest generation of space-based observing instrumentation aboard Hinode and the Solar Dynamics Observatory (SDO) has brought the matter of the ionization state of the plasma firmly to the forefront. It is timely to consider exactly what emission current instruments would detect when observing a corona heated impulsively on small-scales by nanoflares. Only after we understand the full effects of nonequilibrium ionization can we draw meaningful conclusions about the plasma that is (or is not) present.

We have therefore performed a series of hydrodynamic simulations for a variety of different nanoflare properties and initial conditions. Our study has led to several key conclusions. 1. Deviations from equilibrium are greatest for short-duration nanoflares at low initial coronal densities. 2. Hot emission lines are the most affected and are suppressed sometimes to the point of being invisible. 3. The emission detected in all of the SDO-AIA channels is generally dominated by warm, over-dense, cooling plasma. 4. It is difficult *not* to create coronal loops that emit strongly at 1.5 MK and in the range 2 to 5 MK, which are the most commonly observed kind, for a broad range of nanoflare scenarios. 5. The Fe XV (284.16 \AA) emission in most of our models is about 10 times brighter than the Ca XVII (192.82 \AA) emission, consistent with observations. Our overarching conclusion is that small-scale, impulsive heating inducing a nonequilibrium ionization state leads to predictions for observable quantities that are entirely

consistent with what is actually observed.

Subject headings: Sun: corona

1. Introduction

The solar corona is an inhomogeneous plasma, composed of regions differing in terms of their temperature, density and dynamic behaviour, threaded by magnetic field lines. There are open regions, where the magnetic field lines may extend far into interplanetary space, and closed regions, where the magnetic fields that arc above the solar surface are anchored (or line-tied) at both ends in the solar photosphere (where $\beta \gg 1$). In this paper we will focus on closed regions and especially distinct structures called coronal loops, where charged particles clearly follow the arcing magnetic field lines and emit strongly at EUV and X-ray wavelengths. A major question in solar astrophysics concerns how this emission arises. Phrased more conventionally: how is the closed solar corona heated to the million degree temperatures that are necessary to explain the observed EUV and X-ray emission? In this paper we will address the observable consequences of heating in coronal loops. In particular, we will predict the emission intensity (for an extended wavelength range) as though it were measured by the Extreme Ultraviolet Imaging Spectrometer (EIS) on Hinode and the Atmospheric Imaging Assembly (AIA) on the Solar Dynamics Observatory (SDO) for a variety of impulsive heating scenarios. Our aim is to identify the dominant components of the emission from a loop comprising many unresolved strands, each strand at a different stage in its evolution, and to determine the circumstances under which an unambiguous signature of such heating, the “smoking gun” of > 5 MK plasma, could be detected. Our motivation for carrying out this work concerns the possibility of misinterpreting observational data when making claims for or against the impulsive heating scenario. This may be particularly relevant to the analysis of SDO-AIA data due to the instrument’s broad (relative to a spectrometer) wavelength sensitivity in each of its channels and due to the potential for a nonequilibrium ionization state being induced by impulsive heating. Each channel has been chosen for its sensitivity to a specific, dominant emission line, formed at a particular temperature in equilibrium. The relatively broad wavelength sensitivity of each channel means, however, that even channels chosen to observe “hot” emission may also observe nearby lines associated

with significantly cooler emission (the Fe XII line at 195 Å and a nearby Fe VIII line is one well-known example from TRACE). A loop composed of many sub-resolution strands may have just such a profile of hot, warm and cool emission due to each strand being at a different stage in its evolution. A nonequilibrium ionization state further means that the ions emitting the lines that the hot channels have been designed to detect may not even be formed, and in such cases the observed emission is then certain to be dominated by cooler lines that happen to fall within the channel’s wavelength range. Clearly this can lead to significant ambiguity in the interpretation of the observationally gathered data (Golub et al. 1989). We aim to flag these ambiguities by combining imaging and spectroscopic observations, and thereby demonstrate how to avoid the potential pitfalls so that robust and reliable conclusions regarding coronal heating may be drawn.

Early ideas, associated with the Skylab era, held that coronal loops are static equilibrium structures maintained by a constant supply of heat. Such steady (or quasi-steady) heating remains a possible, though not unique, explanation for the appearance of many hot (> 2 MK) X-ray loops. A suitable explanation for warm (~ 1 MK) EUV loops, however, has presented a far greater challenge because they have a number of important properties that are simply incompatible with static equilibrium (Klimchuk 2006, 2009; Klimchuk et al. 2010). In particular: their densities are too great given their associated temperatures and lengths; their field-aligned temperatures are too uniform when measured from imaging observations with the filter ratio technique; and their intensities decrease more slowly with height than would be predicted for a hydrostatic structure. There have been attempts to explain these properties by using models with steady siphon (foot-point to foot-point) flows (Winebarger et al. 2002; Patsourakos et al. 2004) and by inducing conditions of thermal nonequilibrium (Klimchuk et al. 2010), which have proven unsatisfactory.

One idea that has met with a degree of success is that of impulsive heating in loops composed of bundles of unresolved magnetic strands (Cargill 1994; Warren et al. 2002; Klimchuk 2006).

The heating events take place on individual strands and the summed emission from all of the strands in the bundle constitutes the total emission from the loop. The term *nanoflare*, associated with the flux braiding concept of Parker (1988), is often invoked to describe this manner of heating, though we choose to interpret it more broadly as an umbrella term for all mechanisms that produce an energy release on short temporal and small spatial scales. The evolution of a single strand subject to an impulsive heating event is well known. Briefly, impulsive heating lasting for just a few seconds to several minutes causes the coronal temperature to increase rapidly to values > 5 MK. This gives rise to a strong downward heat flux, which has two consequences: (1) the coronal plasma cools rapidly after the heating event ends; and (2) unable to radiate the excess energy away quickly enough, the chromosphere is heated to coronal temperatures and expands, leading to a high-speed evaporative upflow which fills the loop with plasma. There is a significant delay between the time at which the temperature peaks and the time of maximum density. At its peak temperature the loop is underdense compared with a hydrostatic loop of the same temperature and length. Considerable cooling by thermal conduction takes place before the loop density approaches its maximum value. Radiation and enthalpy-driven cooling then take over as the dominant cooling mechanisms (Bradshaw and Cargill 2005, 2010) and the strand enters an extended period of slow cooling and draining of material. During this time the loop is overdense compared with a hydrostatic loop of the same temperature and length. Strands in all of the aforementioned stages of evolution are expected to contribute to the total observed emission from the loop, which is therefore a mixture of the emission from hot, warm and cool strands.

The success of the impulsive heating model at explaining how a warm loop may come to be over-dense (Spadaro et al. 2003) and under-dense hot loops (Porter and Klimchuk 1995) is encouraging and may certainly be considered as indirect evidence of an impulsive heating mechanism operating in the solar corona. However, it is a lack of direct observational evidence that has been the major obstacle to general acceptance of the impulsive heating paradigm. The two most important pieces of observational evidence that together would provide the smoking

gun of impulsive heating are the presence of hot plasma (> 5 MK) and high-speed evaporative upflows. We now review the current state of knowledge relating to the presence of each of these pieces of evidence in turn.

The peak temperatures produced by impulsive heating events are unknown. This is because the magnitude of the energy release is also unknown and is in fact likely to encompass a range of possible values (where the event frequency is related to the magnitude of energy release via a power-law), though the term *nanoflare* (one possible impulsive heating mechanism) was coined due to its estimated energy release of approximately one-billionth the energy released in a full-scale flare. Nonetheless, in order to produce the observed excess densities in loops of temperature around 1 MK the peak temperature must reach at least 5 MK before the onset of cooling. The detection of plasma at temperatures significantly greater than 5 MK would be extremely strong evidence in favour of the impulsive heating scenario because the required energy provision by steady-heating would be extreme, and the observational consequences for both AC-type and DC-type heating would easily be detected, but are not (Schmelz et al. 2009a).

A certain amount of observational evidence for the presence of very hot plasma has been reported, but the emission is faint and has consequently proven difficult to verify. By analysing observations in the multiple filters of the X-Ray Telescope (XRT) on Hinode, Reale et al. (2009a) found evidence for plasma near 10 MK and Schmelz et al. (2009a) found signatures of even higher temperature emission. The findings of Reale et al. (2009a) at the high temperature limit were shown to be consistent with co-temporal RHESSI hard X-ray observations (Reale et al. 2009b) whereas those of Schmelz et al. (2009a) were not, suggestive of a problem in the latter's constraint of the high temperature limit. A follow-up study by Schmelz et al. (2009b) to include RHESSI data constrained the highest temperature emission to be near 10 MK, in agreement with Reale et al. (2009a,b) (see also McTiernan 2009). More recently Sylwester et al. (2010) found evidence for a faint 10 MK component of emission, about 3 orders of magnitude weaker than

the strongest emission between 2 and 3 MK, using the RESIK instrument on the CORONAS-F satellite. This body of work provides the first significant evidence for the presence of 10 MK plasma in quiescent (non-flaring) active regions and indicates that it may be up to 3 (or more) orders of magnitude fainter than the peak of the EM curve at about 3 MK. O'Dwyer et al. (2010) found extremely faint emission in Fe XXIII as observed by Hinode-EIS, suggesting a strongly reduced EM at 14 MK. The faint nature of the hot emission is in fact a further prediction of the models and there are two main reasons. The first is that impulsive heating is expected to take place in the corona under relatively low-density conditions. The short heating time-scales and the relatively long time-scale for the consequent evaporation of chromospheric material into the corona means that significant cooling by thermal conduction can occur (thermal conduction is more efficient in lower density plasma) after the peak temperature has been reached and before the coronal density can increase sufficiently for any direct observations of high temperature emission to be made with a good enough signal to noise ratio. The second reason is also related to the corona being a relatively tenuous medium and the assumption of ionization equilibrium. Under conditions of equilibrium the ionization balance of a plasma is strongly dependent on its electron temperature. However, when the electron temperature changes on time-scales much shorter than the collisional ionization time-scale (the time-scale for the creation of increasingly highly charged ions of the emitting elements) the ionization state of the plasma can become entirely decoupled from the electron temperature. Short heating time-scales lead to rapid temperature increases with which the change in ionization state is unable to keep pace, and when the peak temperature is reached the plasma generally contains many more ions in lower charge states and fewer ions in highly charged states than would be the case at the same temperature in equilibrium. Therefore, the emission from the highly charged ions that would be a signature of the presence of hot plasma is either extremely weak or possibly non-existent. See Bradshaw and Cargill (2006); Reale and Orlando (2008); Bradshaw (2009) for a more detailed elucidation of these issues.

The evidence for high-speed evaporative upflows in quiescent active regions is even

more sparse than the evidence for 10 MK emission. The main findings are due to Hara et al. (2008) and De Pontieu et al. (2009), but their measurements are restricted to emission lines with formation temperatures < 2 MK whereas emission from blue-shifted (upflowing) lines formed at significantly higher temperatures is also required to provide a complete observational picture before detailed comparisons with model predictions of the flow structure can be made (Patsourakos and Klimchuk 2006). Though models do predict upflows exceeding 100 km s^{-1} in some cases, the reason for the paucity of observations is due to the fact that, again, the associated emission is expected to be faint compared with the higher density emission associated with the downflows of the extended radiative and enthalpy-driven cooling and draining phase. In a spatially unresolved observation any upflows would appear as an enhancement in the blue wing of an otherwise red-shifted emission line (Patsourakos and Klimchuk 2006), a signature that is not trivial to disentangle from the signature of the bulk flow. Patsourakos and Klimchuk (2006) computed synthetic line profiles for Ne VIII (770 \AA), Mg X (625 \AA) and Fe XVII (254 \AA) formed at 0.6, 1.2 and 5.0 MK, respectively, and found that the blue wing enhancement in the Ne and Mg lines would be essentially undetectable, and that a clear signature should exist in the blue wing of the Fe line for a certain range of nanoflare energies. This emphasises the importance (indicated above) of having observational velocity measurements across a wide range of coronal temperatures. However, the possibility of a nonequilibrium ionization state being induced in the plasma and its consequences for the formation temperature of the diagnostic emission lines must be raised once again. Patsourakos and Klimchuk (2006) (who did not consider nonequilibrium ionization) found that for a strong upflow signature to be produced, the emission line must be “tuned” to the temperature of the strand leg during the period of evaporation. This means that all of the plasma conditions favourable to the formation of the particular emission line must be met. Since the effective ionization temperature (the temperature of the equilibrium ionization state most closely matching the current ionization state) can lag behind the electron temperature if the heating timescale is shorter than the collisional ionization timescale, it could be the case that

Mg X, for example, is most abundant when the temperature of the strand leg is far higher than its equilibrium formation temperature of 1.2 MK. If the abundance of Mg X were to peak when the electron temperature of the upflowing plasma reaches 5 MK then its line profile might exhibit a clear blue wing enhancement, perhaps rather than the line profile of the Fe XVII line.

As indicated at the beginning of this Introduction, we will focus upon an investigation into the dominant components of the emission, as though observed by Hinode-EIS and SDO-AIA, for a number of plausible impulsive heating scenarios. We defer a detailed study of the dominant line-shift and line wing enhancement signatures associated with impulsive heating to a forthcoming paper.

Our investigation is predicated upon the following chain of reasoning. Given that models predict hot (> 5 MK) plasma should be a signature of impulsive heating, one would expect to see hot emission in the appropriate channels of observing instruments such as SDO-AIA, which specifically includes channels chosen for their sensitivity to very hot emission (Fe XVIII at 94 Å, Fe XXIII at 131 Å and Fe XXIV at 193 Å). However, the detectability of such emission depends upon several very important properties of the heating event (Bradshaw and Cargill 2006; Reale and Orlando 2008) and also upon the properties of the plasma prior to heating. In fact, a crucial question is: what is the state of the plasma at the heating location before it is heated? The answer to this question matters for several reasons:

1. if the initial density is low then the magnetic reconnection rate is presumably fast (dependent upon the Alfvén speed), and if the plasma is heated by a reconnection-based mechanism then the density determines the rate and duration of heating;
2. if the initial density is low then the plasma can quickly be heated to high temperatures due to the relatively large amount of energy released per particle;
3. if the initial density is low and the duration of heating is short then cooling by efficient

thermal conduction takes place before chromospheric evaporation can supply a significant amount of material to the corona, and the emission measure at the highest temperatures is then very low;

4. if the density is low and the duration of heating is short then the effective ionization temperature remains much lower than the electron temperature during heating and during cooling by efficient thermal conduction, and the emission measure at the highest inferred temperatures is then very low or possibly even zero if an observer constructs an emission measure by incorrectly assuming an equilibrium ionization state;
5. if the emission measure at the highest temperatures is very low then in the multi-stranded case the emission will be dominated by the higher density, lower temperature component from the long radiative and enthalpy-driven cooling and draining phase.

Therefore we may ask: what are we actually seeing in the SDO-AIA channels? Is it the target hot emission for which the channel was ostensibly chosen? Is it cooler emission that also happens to fall within the wavelength sensitivity of the channel?

Our strategy for answering these questions is to investigate combinations of initial plasma conditions and properties of the impulsive heating in order to predict the circumstances under which hot emission (and thus a direct signature of heating) may be observed and confirmed. We predict the dominant components (cool, warm or hot) and the intensity of the emission as though detected by SDO-AIA for each of the combinations we investigate, and we then determine whether Hinode-EIS would detect sufficient hot emission in order to unambiguously confirm the detection of hot plasma by SDO-AIA. We proceed by describing the numerical model and experiments in Section 2, and the forward modeling procedure in Section 3. We present and discuss our results in Section 4, and provide a summary and conclusions, together with our intentions for future work, in Section 5.

2. Numerical model and experiments

We solve the one dimensional hydrodynamic equations appropriate for modeling a single coronal strand along the magnetic field. The diameter of the strand is assumed to be far smaller than can be resolved by any observing instrument. We describe our procedure for reconstructing the emission from a loop composed of many sub-resolution strands in Section 3. Since in certain cases we are interested in heating initially tenuous strands to temperatures in excess of 10 MK we require separate equations for the electron and ion fluids, assuming that one or the other species is directly heated and they are only weakly collisionally coupled in a tenuous atmosphere. For the purposes of the current work we preferentially heat the electrons, though see Longcope and Bradshaw (2010) for an alternative scenario. We further assume quasi-neutrality ($n_e = n_i = n$) and current free ($v_e = v_i = v$) conditions. The conservative forms of the mass and momentum equations are then

$$\frac{\partial \rho}{\partial t} = -\frac{\partial (\rho v)}{\partial s}, \quad (1)$$

$$\frac{\partial (\rho v)}{\partial t} = -\frac{\partial (\rho v^2)}{\partial s} - \frac{\partial (p_e + p_i)}{\partial s} + \frac{\partial}{\partial s} \left(\frac{4}{3} \mu_i \frac{\partial v}{\partial s} \right) + \rho g_{\parallel}, \quad (2)$$

where t and s are time and the field-aligned spatial coordinate, ρ is the ion mass density ($m_e \ll m_i$), v the bulk velocity of the flow and g_{\parallel} the field-aligned gravitational acceleration. Though we will write separate electron and ion energy equations we assume that collisions between like-species are frequent enough that the electron and ion pressures are $p_e = k_B n T_e$ and $p_i = k_B n T_i$. The penultimate term on the right-hand side of Equation 2 is the viscous contribution to the ion momentum (the electron viscosity would be smaller by a factor $m_e/m_i \ll 1$ and is thus neglected). Viscosity is expected to become extremely important at the high temperatures our experiments reach and so must be included in the strand physics. The internal electron energy is

$E_e = \frac{1}{\gamma-1} p_e$ (electron kinetic energy is negligible in comparison) and is determined by

$$\frac{\partial E_e}{\partial t} = -\frac{\partial}{\partial s} [(E_e + p_e) v] + v \frac{\partial p_e}{\partial s} + \frac{\partial}{\partial s} \left(\kappa_{e0} T_e^{\frac{5}{2}} \frac{\partial T_e}{\partial s} \right) + \frac{1}{\gamma-1} k_B n \nu_{ei} (T_i - T_e) - E_R + E_H, \quad (3)$$

where κ_{e0} is the coefficient of electron thermal conductivity, $\gamma = \frac{5}{3}$ and ν_{ei} is the electron-ion collision frequency. The first term on the right-hand side of Equation 3 represents the energy transported as an enthalpy flux. The second term describes the work done by the electric field (there is a small charge imbalance), where the electron pressure is substituted from the electron momentum equation by replacing the electric field term

$$eE = -\frac{1}{n} \frac{\partial p_e}{\partial s}. \quad (4)$$

The third term on the right-hand side of Equation 3 is the energy transport due to thermal conduction and the fourth term is the energy collisionally lost (gained) to (from) the ion fluid when $T_e > T_i$ ($T_e < T_i$). The fifth term, E_R , represents the volumetric radiative energy loss due to line emission (predominantly at EUV temperatures) and bremsstrahlung (at higher temperatures). In the current work we calculate the contributions to E_R from the elements H, He, C, N, O, Ne, Na, Mg, Al, Si, S, Ar, Ni using the Chianti atomic database (Dere et al. 1997; Landi et al. 2006) and the assumption of ionization equilibrium. The contribution to E_R from Ca and Fe is calculated from (for Fe)

$$E_{R(\text{Fe})} = n^2 \left(0.83 \times \text{Ab}(\text{Fe}) \times \sum_{i=1}^{27} \epsilon_i Y_i \right), \quad (5)$$

where 0.83 is the proton:electron ratio, $\text{Ab}(\text{Fe})$ is the iron abundance relative to hydrogen, the summation is performed over all of the ionization states of Fe (neutral to fully ionized), ϵ_i is the combined emissivity from all the lines of charge state i (in spectroscopic notation $i = 1$ is neutral

iron, commonly denoted Fe I) calculated by Chianti and Y_i is the time-dependent population fraction of charge state i which is found by solving the coupled system of equations

$$\frac{\partial Y_i}{\partial t} = -\frac{\partial(Y_i v)}{\partial s} + n(I_{i-1}Y_{i-1} + R_iY_{i+1} - I_iY_i - R_{i-1}Y_i), \quad (6)$$

where I and R are temperature dependent ionization and recombination rates, respectively, and the normalising condition for Equation 6 is $\sum_{i=1}^{27} Y_i = 1$. For Ca the summations are performed for $i = 1$ to 21 since its atomic number is 20. Thus the volumetric radiative emission from Ca and Fe can be accurately calculated when the ionization state departs from equilibrium. We chose to only treat the elements Ca and Fe in this way because we are primarily interested in the emission from Fe, which dominates the coronal emission spectrum, and from Ca which contains a particularly useful diagnostic line at 192.82 Å. Solving Equations 5 and 6 for fewer elements also significantly reduces computational demands and run-times. We note that deviations from equilibrium are only significant at times when radiation plays a very minor role in the energy balance, so the effect on the plasma thermodynamics is extremely small.

Finally, the sixth term, E_H , is the volumetric energy input due to impulsive heating. The spatial profile of E_H is such that it is uniform along the magnetic field and its temporal envelope is a sudden switch-on with constant heating for t_H s before a sudden switch-off. Alternative heating models may ramp up the energy input to its maximum value over a particular time-scale (and similarly decay to zero), but the key property for our purposes is simply that it be impulsive.

The ion energy is $E_i = \frac{1}{\gamma-1}p_i + \frac{1}{2}\rho v^2$ (only the ions contribute to the kinetic energy of the plasma) and is determined by

$$\frac{\partial E_i}{\partial t} = -\frac{\partial}{\partial s} [(E_i + p_i) v] - v \frac{\partial p_e}{\partial s} + \frac{\partial}{\partial s} \left(\kappa_{i0} T_i^{\frac{5}{2}} \frac{\partial T_i}{\partial s} \right) + \frac{1}{\gamma-1} k_B n v_{ei} (T_e - T_i) + \frac{\partial}{\partial s} \left(\frac{4}{3} \mu_i v \frac{\partial v}{\partial s} \right) + \rho v g_{\parallel}, \quad (7)$$

where the penultimate term is the viscous term with components that describe the work done by

the viscous stress on the bulk flow and the energy lost to irreversible heating.

We use the numerical code HYDRAD (Bradshaw and Cargill 2010, and references therein) to solve the two-fluid hydrodynamic equations described above. HYDRAD has several desirable features which make it ideal for application to the study of impulsive heating to extremely high temperatures. Written exclusively in C++, it is fast and robust, and models an entire loop strand (foot-point to foot-point for any geometry via an analytical equation, or look-up table, for gravity) with an adaptive grid for efficiently capturing small-scale properties of the solution. It can handle multi-species fluids, solves the time-dependent ionization state equations / calculates the nonequilibrium volumetric radiative emission for the set or subset of elements from H to Ni ($Z=1$ to 28), and incorporates a flexible, parameterised heating function which enables the energy release of different heating mechanisms to be emulated (for electrons and ions). It is user-friendly and easily configurable via a Java-developed graphical user interface.

We conduct 14 numerical experiments with properties that are summarised in Table 1. The first column indicates the number assigned to each Run, which will be used to reference them as they are discussed in turn. The second, third and fourth columns describe the initial, hydrostatic equilibrium state adopted for each run, prior to the impulsive heating event. The loop length $2L$ is defined as the transition region to transition region foot-point length. The computational domain also includes a deep (many scale heights) chromosphere at 2×10^4 K that is attached to each transition region foot-point in order to provide a source of material to evaporate into the corona upon heating. $n_a(t = 0)$ and $T_a(t = 0)$ are the initial apex number density and species temperature respectively (in hydrostatic equilibrium, $T_e = T_i$). The fifth and sixth columns describe the properties of the impulsive heating event. H and t_H are the volumetric heating rate (applied uniformly along the strand) and the duration of heating. The final three columns describe the properties of the strand at the end of the period of impulsive heating. $n_a(t = t_H)$ is the apex number density and $T_{a(e,i)}(t = t_H)$ are the apex electron and ion temperatures.

Table 1: A summary of the numerical experiments relating to: the initial plasma conditions [$2L$, $n_a(t = 0)$, $T_a(t = 0)$]; the properties of the impulsive heating events [H , t_H]; and the apex density, and the electron and ion temperatures reached at the end of heating [$n_a(t = t_H)$, $T_{a(e)}(t = t_H)$, $T_{a(i)}(t = t_H)$].

#	$2L$	$n_a(t = 0)$	$T_a(t = 0)$	H	t_H	$n_a(t = t_H)$	$T_{a(e)}(t = t_H)$	$T_{a(i)}(t = t_H)$
	[Mm]	[cm ⁻³]	[MK]	[erg cm ⁻³ s ⁻¹]	[s]	[cm ⁻³]	[MK]	[MK]
1	20	10^7	0.15	0.05	10	2.2×10^7	4.60	0.16
2	20	10^8	0.38	0.10	10	1.3×10^8	4.80	0.41
3	20	10^8	0.38	0.10	30	6.0×10^8	5.20	0.71
4	20	10^8	0.38	0.10	100	3.2×10^9	6.00	5.40
5	20	10^8	0.38	0.10	300	2.4×10^9	5.80	4.60
6	20	10^9	1.10	1.00	10	1.3×10^9	9.10	1.30
7	20	10^9	1.10	1.00	30	7.1×10^9	10.0	9.50
8	20	10^9	1.10	5.00	10	1.3×10^9	14.0	1.20
9	80	10^8	0.93	0.10	10	1.3×10^8	10.6	0.94
10	80	10^8	0.93	0.10	30	1.3×10^8	10.4	0.99
11	80	10^8	0.93	0.10	100	1.6×10^9	11.2	16.0
12	80	10^8	0.93	0.10	300	5.1×10^9	11.0	12.0
13	80	10^9	1.80	1.00	10	8.1×10^8	20.3	1.90
14	80	10^9	1.80	1.00	30	8.2×10^8	19.8	2.10

3. Forward modeling of observed emission

The seemingly monolithic structures that are observed as coronal loops are generally thought to be composed of many individual strands (Cargill and Klimchuk 1997; Aschwanden et al. 2000; Reale and Peres 2000; Warren et al. 2002) with transverse (to the magnetic field direction) scale lengths far smaller than any observing instrument can resolve. It is unclear precisely how many sub-resolution strands exist in a single resolution element and estimates vary from tens to thousands. Clearly, modeling every strand individually is not an efficient, economical or indeed realistic use of computational resources given that a single run can take from minutes to days depending upon the desired detail of treatment (a full nonequilibrium ionization calculation, for example), grid resolution, and so on. We therefore construct a composite loop bundle by carrying out a model run for a single strand and assuming that each stage in the evolution of that strand corresponds to a single snapshot in time of the state of a unique strand. For example, if we evolve the strand for 1000 s of solar time and read the state of the strand every second then we obtain 1001 (0 - 1000 s) unique temperature, density, bulk velocity (etc.) profiles, which we may assume correspond to 1001 different strands comprising the full loop. Thus, we tacitly assume at each instant when we observe a loop that it is composed of many strands, each representing one of every (or at least many) possible state encountered during the heating and cooling of a single strand. We expect this treatment to be valid if there are a statistically significant number of strands, if they individually evolve in a similar manner, and if the loop is sufficiently long-lived such that at least one (or a few) of the strands have undergone a complete cycle of heating and cooling. Phrased differently, we assume a storm of similar nanoflares that lasts at least as long as the strand cooling time (Klimchuk 2009).

We begin the forward modeling process with geometrical considerations. We first assume that the loop describes a semi-circle as the field is traced from foot-point to foot-point. Secondly, we choose a characteristic diameter for the cross-section (assumed to be circular) of the loop

bundle, which for the present work we arbitrarily take to be 0.5'' or about 380 km (approximately the size of a single SDO-AIA pixel and half the width of the highest resolution Hinode-EIS slit of 1''). Taking the above example of 1001 elementary strands comprising the loop then each strand has a cross-section of $114000 \text{ km}^2 / 1001 \approx 114 \text{ km}^2$ and a diameter of about 12 km. The emission from the loop is the summed emission from 1001 individual strands of this size. Note that the diameter of the strands is not critical. We could assume larger or smaller strands by sampling the simulation less or more frequently than once every second. Thirdly, the loop is assumed to be located at the disk center and oriented perpendicularly to the solar surface, with the plane of the loop aligned in the East-West direction. Thus, the line-of-sight lies parallel to the plane of the loop and the loop itself is observed from directly above. This is a geometrical convenience so that the spatial emission profile along the loop can be binned into a single row of detector pixels, though it does have the consequence that the curvature of the loop leads to an increase in the line-of-sight depth of the emitting plasma towards the foot-points, which increases their brightness relative to the foot-points of the same loop oriented at some angle < 90 degrees to the solar surface.

The next step is to select the instruments of interest, obtain the appropriate response functions and determine which ions emit spectral lines within their wavelength sensitivity ranges. We have chosen to focus on Fe (the dominant contributor to the coronal emission spectrum) and forward model the expected emission from our loops in the 94, 131, 193, 211 and 335 Å channels of SDO-AIA, the 195 Å channel of TRACE (for a sensitivity comparison with SDO-AIA) and for a selection of Hinode-EIS lines.

The intensity of a line expressed as a data number count rate ($\text{DN pixel}^{-1} \text{ s}^{-1}$) is given by

$$I(\lambda, n, T) = \frac{G(\lambda) \times 0.83 \times Ab(Y) \times Y_i \times \epsilon(\lambda, n, T) \times \langle EM \rangle}{4\pi \times (hc/\lambda)}, \quad (8)$$

where hc/λ is the photon energy (units: erg), $G(\lambda)$ is the instrument response function (units: $\text{DN pixel}^{-1} \text{ photon}^{-1} \text{ sr cm}^2$), 0.83 is the proton:electron ratio, $Ab(Y)$ is the abundance (relative to

hydrogen) of element Y , Y_i is the population fraction of charge state i of element Y , $\epsilon(\lambda, n, T)$ is the emissivity of the line (units: $\text{erg s}^{-1} \text{cm}^3$) calculated using the EMISS_CALC function provided by Chianti, and $\langle EM \rangle$ is the spatially averaged column emission measure in the pixel (units: cm^{-5}):

$$\langle EM \rangle = \frac{EM_{pix}}{A_{pix}}, \quad (9)$$

where $EM_{pix} = n_e^2 dV$ is the emission measure in the pixel and A_{pix} is the pixel area. The instrument response function, $G(\lambda)$, is the product of the effective area, plate scale, and gain of the instrument. For EIS we use response functions obtained from SolarSoft. For AIA, we use $8.46 \times 10^{-2} \text{ sr pixel}^{-1}$ for the plate scale, 18 electron DN^{-1} for the gain, and effective area data (units: $\text{cm}^2 \text{ electron photon}^{-1}$) kindly provided by Mark Weber. Table 2 lists all of the Fe ions that emit within the wavelength sensitivity ranges of the imaging instrument (AIA and TRACE) channels, which of those ions emit the strong high temperature lines that a number of the channels have been specifically chosen to detect in the search for hot plasma, and the Hinode-EIS lines that we have also chosen for our study. These ions were identified using the Chianti atomic database.

The emission intensity from the grid cell is then added to the total for the appropriate detector pixel(s). This is determined by projecting the grid cell onto a two-dimensional plane oriented perpendicularly to the line-of-sight (so extending in the solar X (E-W) and Y (N-S) directions with constant Z) representing the detector, calculating the position and the extent of the cell in the X direction (recall that we assume the loop is aligned E-W and so the Y coordinate remains constant), and finally the proportion of its emission that it contributes to each pixel that it intersects (a grid cell could be wider than a single pixel). This procedure is repeated for all of the spectral lines of the ions, for all of the grid cells of the strand, and for every strand comprising the loop. For the Hinode-EIS lines the procedure is carried out for just a single spectral line. The result is then a prediction of the total emission along the loop, due to the contributions from the many

Table 2: A summary of all the emitting ions, and those that the emit strong hot lines which certain of the channels have been centered on, in the wavelength sensitivity ranges of the instrument channels used in the present work. This summary was compiled using Chianti. The symbol ^d denotes a dielectronic satellite line.

Instrument / Channel (Å)	All Ions	Hot Ions
SDO-AIA / 94	Fe VIII, IX, X, XII, XV, XVII, XVIII, XIX XX, XXI, XXII, XXIII	Fe XVIII
SDO-AIA / 131	Fe VIII, IX, X, XI ^d , XII, XV, XVII, XVIII XIX, XX, XXI, XXII, XXIII	Fe XX, XXIII
SDO-AIA / 193	Fe VIII, VIII ^d , IX, X, XI, XI ^d , XII, XIII XIII ^d , XIV, XV, XV ^d , XVII, XVIII, XIX, XX XXI, XXII, XXIII, XXIV, XXV	Fe XXIV
TRACE / 195	Fe VIII, IX, X, XI, XII, XIII, XIII ^d , XIV XV, XVII, XVIII, XIX, XX, XXI, XXII, XXIII XXIV, XXV	Fe XXIV
SDO-AIA / 211	Fe VIII, VIII ^d , IX, IX ^d , X, XI, XI ^d , XII XIII, XIII ^d , XIV, XV, XVII, XVIII, XIX, XX XXI, XXII, XXIII, XXIV, XXV	Fe XIV
SDO-AIA / 335	Fe VI, VIII, IX, X, XI, XI ^d , XII, XII ^d XIII, XIII ^d , XIV, XIV ^d , XV, XV ^d , XVI, XVI ^d XVII, XVIII, XIX, XX, XXI, XXII, XXIII	Fe XVI, XVI ^d
Hinode-EIS	Fe XI (192.830), XII (195.119), XV (284.163) XVI (262.976), XVII (254.347), XXIII (263.766) Ca XVII (192.820)	

sub-resolution strands at different stages of evolution, that would be measured by a particular observing instrument.

Before concluding this section it is worth noting the computational demands made by the necessity of obtaining a comprehensive spectrum for the forward modeling analysis. Though the forward modeling code developed for our investigations selects only the lines that emit within a specified wavelength range, determined by the sensitivity of each instrument, there can still be many thousands of lines contributing to the emission detected at each pixel. For example, we choose a wavelength range of 40 \AA centered on the wavelength of peak sensitivity for each of the AIA channels, which in the case of the 193 \AA channel requires a total of 3390 emission lines to be included in the calculation. The widths of the instrument response curves vary between channels, but a decrease of at least 2 orders of magnitude from the peak sensitivity at $\pm 20 \text{ \AA}$ from the central wavelength of the channel is usual. This should be sufficient to capture the influence of any particularly strong nearby lines, while achieving a manageable computational load. Repeating these calculations for every spectral line, for every grid cell of every strand that comprises the loop, and for every instrument, is a non-trivial computational task when carrying out a detailed forward modeling study for imaging instruments. For EIS the wavelength range is chosen such that the only selected line is the one of direct interest to us, which reduces the computational demands by orders of magnitude.

4. Results

4.1. Short loops

In this section we discuss the results of our numerical experiments for relatively short loops of $2L = 20 \text{ Mm}$ (transition region foot-point to transition region foot-point length). In the first of our numerical experiments (Run 1 in Table 1) a spatially uniform, impulsive heating event of

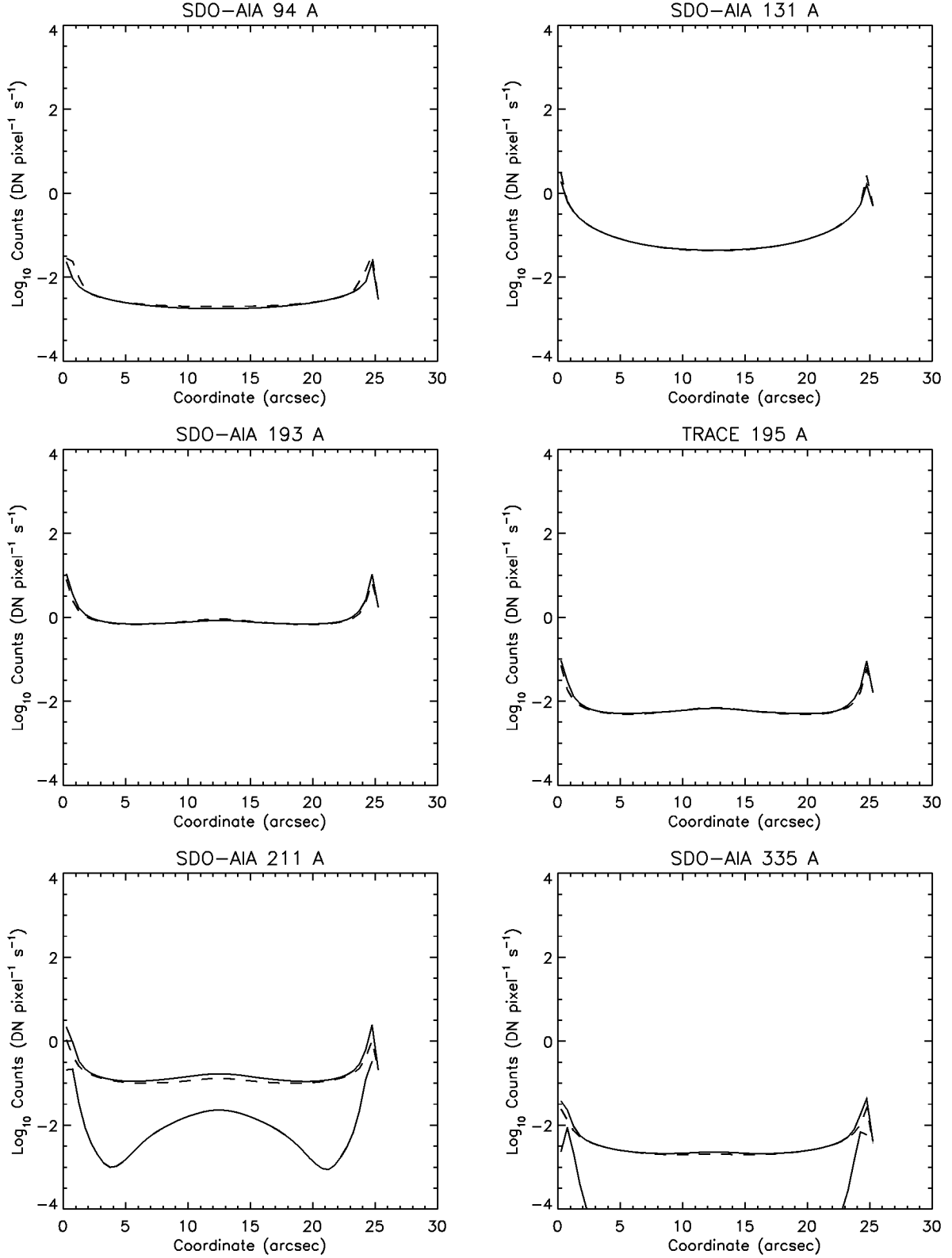


Fig. 1.— Synthesised total emission (upper pair of curves in each panel) and hot emission only (lower pair of curves in each panel) along the multi-stranded loop corresponding to Run 1 in a selection of SDO-AIA channels and the TRACE 195 Å channel. Solid lines denote equilibrium ionization and dashed lines nonequilibrium.

10 s duration releases approximately 10^9 erg cm^{-2} into the strand. This corresponds to a total energy input of about 10^{21} erg for a strand of diameter 12 km. The electron (heated particle) temperature increases rapidly, reaching 4.6 MK at 10 s when the heating ends. By comparison, the ion temperature increases by only 0.01 MK from its initial equilibrium temperature ($T_e = T_i = 0.15 \text{ MK}$). The substantial difference between the electron and the ion temperatures demonstrates the dramatic decoupling between the fluid species during this event and that under no circumstances can such heating be modeled by a single-fluid treatment. The ions are expected to gain energy from the electrons via collisions, but the tenuous nature of the plasma leads to long mean-free-paths and collision time scales, which means that by the time the heating ends the ions have gained only a little additional energy from the electrons. This suggests that the collision-dependent ionization state should be similarly affected and we will later show that this is indeed the case. The short heating time scale also means that the event ends before chromospheric evaporation can raise the coronal density into a more collisional regime and so after 10 s the corona is expected to cool extremely rapidly due to highly efficient thermal conduction. By the time the corona fills appreciably its temperature has decreased dramatically and the emission measure for the event is consequently dominated by higher density, low temperature components.

Figure 1 shows the total emission along the composite loop constructed from the results of Run 1 (following the procedure described in Section 3), as would be detected in a selection of SDO-AIA channels and the TRACE 195 Å channel. Each panel of the figure corresponds to a different channel and contains four separate curves, described below. Not all of the curves appear in the panels due to the choice of y-axis scale, which is cut-off at $10^{-4} \text{ DN pixel}^{-1} \text{ s}^{-1}$. At this extreme, exposure times would need to be 10^4 s in order to achieve a single count per pixel, which is considerably longer than the time scales of phenomena of interest to us. It is worth noting here that these values can be scaled by relative changes in the effective line-of-sight depth if the reader is interested in loops of different diameter (a suitable procedure is described in Section 5). Recall that we have assumed a diameter of $0.5''$. The predicted count rates will also change if the delay

between successive nanoflares in a given strand is different from the duration of our runs (1000 s for short loops and 3000 s for long loops).

The first set of curves that are plotted are the total emission due to all of the ions (as listed in column 2 of Table 2) that emit within the wavelength sensitivity range of the channel for equilibrium (solid-line) and nonequilibrium (dashed-line) ionization states. The second set of curves are the emission due only to the ions that emit strong, high temperature lines (as listed in column 3 of Table 2) that fall within the channel’s sensitivity range, again for equilibrium (solid) and nonequilibrium (dashed) ionization states. Note that the ‘hook’ at the right-most extreme of some of the curves, where the counts appear to fall, is an artifact that occurs when the right edge of the loop falls in the middle of a pixel. The left edge of the loop is perfectly aligned with the pixel boundary by convention. It is straightforward to distinguish between the two sets of curves since the total emission from all of the ions is naturally stronger than the emission from the hot ions alone. The question, of course, is how much stronger? Does the cool emission (total emission minus hot emission) dominate? If so, then even emission observed in supposedly hot channels may not in fact be hot and, if misinterpreted, will lead to incorrect conclusions concerning the presence of hot plasma. Similarly, the lack of emission in a hot channel does not necessarily imply that no hot plasma is present, since nonequilibrium effects may greatly reduce the population of high ionization stages even if the kinetic temperature is high. Addressing the conditions which lead to these effects is the primary purpose of our study.

Examining Figure 1 we notice several things. In all of the channels, the emission from hot lines alone is too weak to be detected. Solid curves representing equilibrium ionization exceed the threshold in the 211 and 335 Å channels, but this is an artificial equilibrium that has been assumed. The dashed curves representing realistic nonequilibrium ionization are absent from the plots. Run 1 uses a relatively weak nanoflare—the weakest that we consider—and the peak electron temperature of 4.6 MK is well below the temperatures where the hot lines in the 94, 133,

193, and 195 Å channels are typically formed. The hot lines in the 211 and 335 Å channels (Fe XIV and Fe XVI) are in the right temperature range for detection, but their brightness is limited by the small emission measure and strongly nonequilibrium conditions.

In contrast to the hot lines, the cool lines which dominate the total emission are formed under near equilibrium conditions. This is evidenced by the near overlap of the equilibrium and nonequilibrium curves in Figure 1. The lack of appreciable hot emission and the equilibrium nature of the cool emission indicate that most of the signal, in all channels, comes from strands that are past the heating and rapid thermal conduction cooling phases and have entered the slow phase of radiation/enthalpy cooling and draining. Run 1 is a stark example of how the detection of a signal in the 94 and 131 Å channels, which are normally thought of as ‘hot’ channels, does not necessarily mean that hot plasma is actually present. The channels have strong sensitivity near 10 MK, but they also have strong sensitivity near 1 MK, and it is the cooler plasma that drives the signal in this case.

The ambiguity inherent in AIA and TRACE observations is of course not present in spectrally resolved observations from EIS. Figure 2 shows the emission that would be observed by EIS in a selection of spectral lines covering a range of temperatures. As before, solid and dashed curves represent equilibrium and nonequilibrium ionization, respectively. The relatively cool lines of Fe XI and Fe XII are formed in equilibrium, except at the footpoints, but the remaining lines are both extremely faint and out of equilibrium, consistent with the results for AIA hot lines. Note that the shapes of the (artificial) equilibrium curves for Fe XV and Fe XVI mimic those from the hot lines in the 211 and 335 Å channels, as they should (see Table 2).

Appendices A and B contain tables which provide quantitative numerical estimates for the intensity of the detected emission in each of the AIA channels (Appendix A) and for each of the EIS lines (Appendix B) studied here, for all of the numerical experiments. The exception is for Fe XXIII, which will be shown to make a negligible contribution to the coronal emission for all

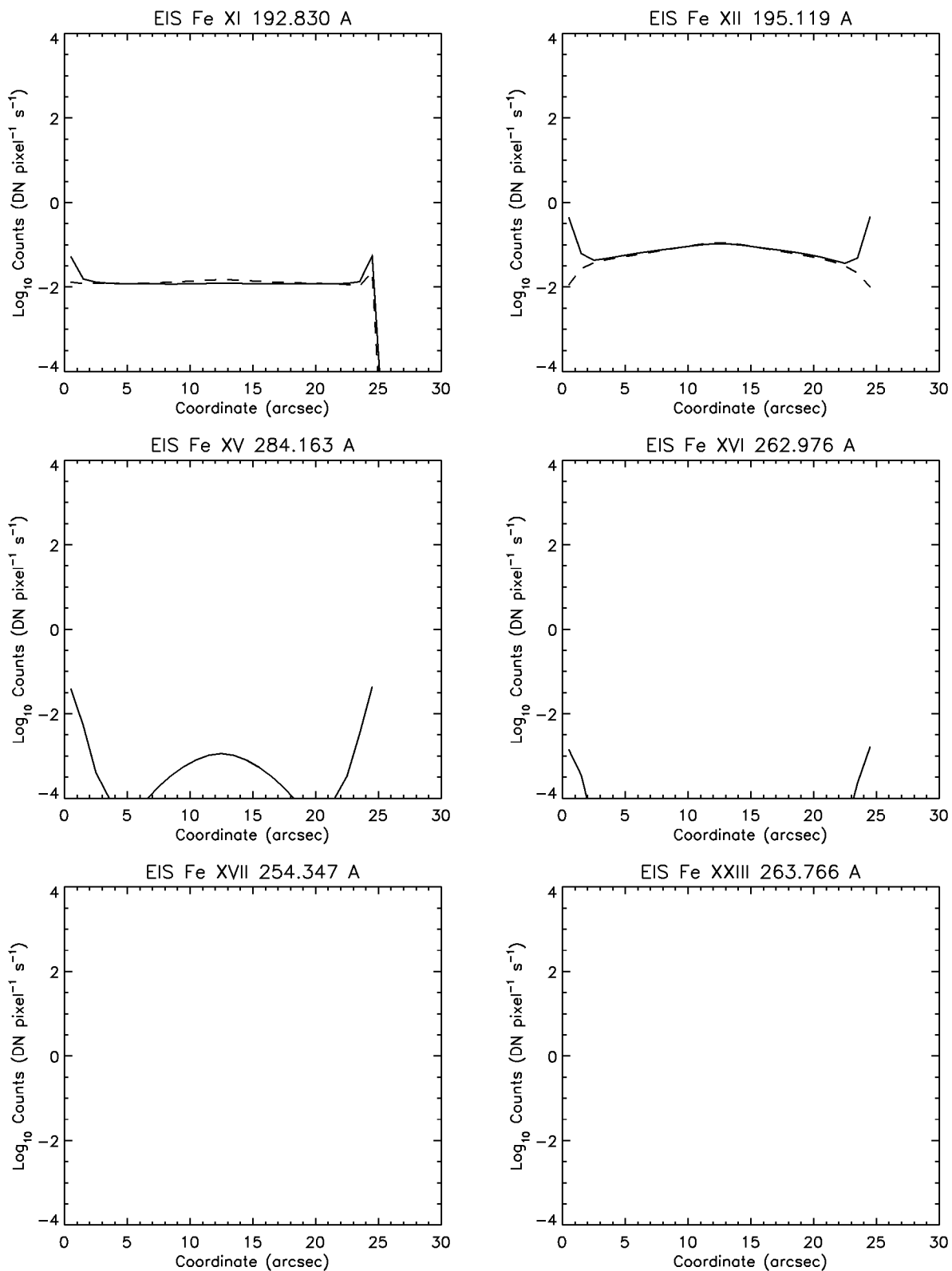


Fig. 2.— Synthesised emission along the multi-stranded loop corresponding to Run 1 for a selection of spectral lines formed at different temperatures as would be observed by Hinode-EIS. Solid lines denote equilibrium ionization and dashed lines nonequilibrium.

of our numerical experiments, and is replaced in the tables pertaining to EIS with an estimate for the Ca XVII line at 192.82 Å, a well-known and frequently studied line. Tables 3 and 4 give the contribution to the emission detected in the AIA channels for the supposed hot ions that emit strong lines within the wavelength sensitivity range of each channel (Table 2). Table 3 provides the apex intensity only and Table 4 the total intensity integrated along the loop. The values calculated assuming ionization equilibrium and nonequilibrium (in brackets) are listed. Tables 5 and 6 give the total emission detected in the AIA channels taking account of all of the emission lines that fall within their wavelength sensitivity ranges. Tables 7 and 8 give the ratios of the detected hot emission to the total detected emission for the quantities listed in Tables 3 to 6 for the equilibrium (Table 7) and nonequilibrium (Table 8) calculations. Tables 9 and 10 give the spectral line intensities detected by EIS at the apex (Table 9) and integrated (Table 10) along the loop. The values calculated assuming ionization equilibrium and nonequilibrium (in brackets) are listed. Table 11 gives the ratios of the detected nonequilibrium to the detected equilibrium emission for the apex and integrated values (in brackets). These tables are provided both as an aid to interpreting each of the figures and also in order that the reader may make quantitative estimates of the likely properties of the detected emission for scenarios of direct interest to them.

Returning to the discussion of the results of our numerical experiments, it is clear that Run 1 is a rather extreme case. The initial density is only 10^7 cm^{-3} at the apex of the loop and the impulsive heating event lasts for just 10 s. However, Run 1 does serve the useful purpose of identifying the range of parameter space that needs to be explored. An even more tenuous set of initial conditions or an even more impulsive heating scenario would make the detection of hot plasma even less likely, so there is little value in pursuing such cases. Runs 2-5 (Table 1) consider less extreme scenarios than Run 1. The initial coronal density increases by an order of magnitude to 10^8 cm^{-3} , the volumetric heating rate doubles, and the duration of the heating progressively increases from 10 s to 30, 100, and 300 s.

For a given heating rate, longer duration nanoflares deposit more energy into the strand and therefore the peak temperature tends to be higher. There is a limit to the temperature increase, however. Once the electron temperature is sufficiently high that thermal conduction cooling balances the heating rate, there is no further increase in temperature. This saturation effect is evident in the second-to-last column of Table 1. The ions behave much differently. Because they gain energy by collision with the electrons and not from direct nanoflare heating, their temperature steadily rises until it matches that of the electrons (last column).

Note that there are small differences in the electron temperature at the end of heating in Runs 2-5 even though the saturation effect described above would suggest that they should be equal. The reason is the following. Nanoflares are violent events that produce high-speed evaporative upflows. When the flows from the two legs collide at the apex they generate large amplitude sound waves and sometimes even rebound shocks. The plasma is not uniform, and conditions at any one spatial point and any one instant in time do not always accurately represent the overall conditions in the strand. Hence, perfectly systematic behavior should not be expected for the $t = t_H$ apex parameters that are given in Table 1.

The saturation of the temperature in Runs 2-5 has several important consequences. First, there is period of relatively constant temperature between when saturation occurs and when the nanoflare ends. This period is obviously longer for longer duration events, and therefore longer nanoflares leave more time for the ion populations to equilibrate before the onset of rapid cooling. Second, longer nanoflares allow more time for evaporation to fill the strand with plasma while the temperature remains high. This both increases the emission measure and further enhances the equilibration of the ion populations, since collision frequencies are higher at greater density. As a consequence of these effects, high temperature lines tend to be brighter for longer duration nanoflares. Our numerical experiments bear this out.

Figures 3 and 4 show the synthesized AIA and EIS intensity profiles for Run 3 ($t_H = 30$ s),

and Figures 5 and 6 show the corresponding profiles for Run 5 ($t_H = 300$ s). Comparing with Figures 1 and 2 (Run 1, $t_H = 10$ s) we see that the hot lines are indeed progressively brighter and contribute progressively more to the total AIA emission as the nanoflare duration increases. The hot lines in the 211, 335, and 94 Å channels as well as the Fe XV, XVI, and XVII lines observed by EIS all reach detectable levels in Run 5, and some do also in Run 3. The hot lines actually dominate the cool lines in the 335 and 94 Å channels for Run 5. The hot lines in the 193 and 195 Å channels and the Fe XXIII EIS line have such high ionization stages that they remain below the detection threshold for all of these runs.

Runs 2 and 4 follow the patterns discussed above. The corresponding AIA and EIS intensity plots can be found in the on-line material.

One factor contributing to the brighter hot emission in Runs 2-5 compared to Run 1 is the increased initial density. This is explored further in Runs 6-8, where the initial density is increased by an order of magnitude to 10^9 cm^{-3} . The nanoflare heating rate is also increased by an order of magnitude to $1 \text{ erg cm}^{-3} \text{ s}^{-1}$ in Runs 6 and 7 and to $5 \text{ erg cm}^{-3} \text{ s}^{-1}$ in Run 8. The stronger heating rate results in a higher peak temperature, near 10 MK, which scales approximately as $H^{2/7}$ when the heat flux is not saturated. Both the higher initial density and higher peak temperature produce brighter emission in the hot lines. Figures 7 and 8 show the AIA and EIS intensity profiles for Run 7. This run is best compared with Run 3 (Figures 3 and 4), which also has a nanoflare duration of 30 s. The most notable differences are that, in Run 7, the hot lines are in equilibrium and dominate the total signal in the 94 Å channel, and the EIS Fe XVII line is now above the detectable threshold.

The importance of the initial density is best seen in the ion kinetic temperature at the end of heating (last column of Table 1). In Run 3 the ion and electron temperatures are much different, but in Run 7, which has the higher initial density, the ion and electron temperatures are nearly the same. This is true even though the temperatures are higher in Run 7 and in principle should be

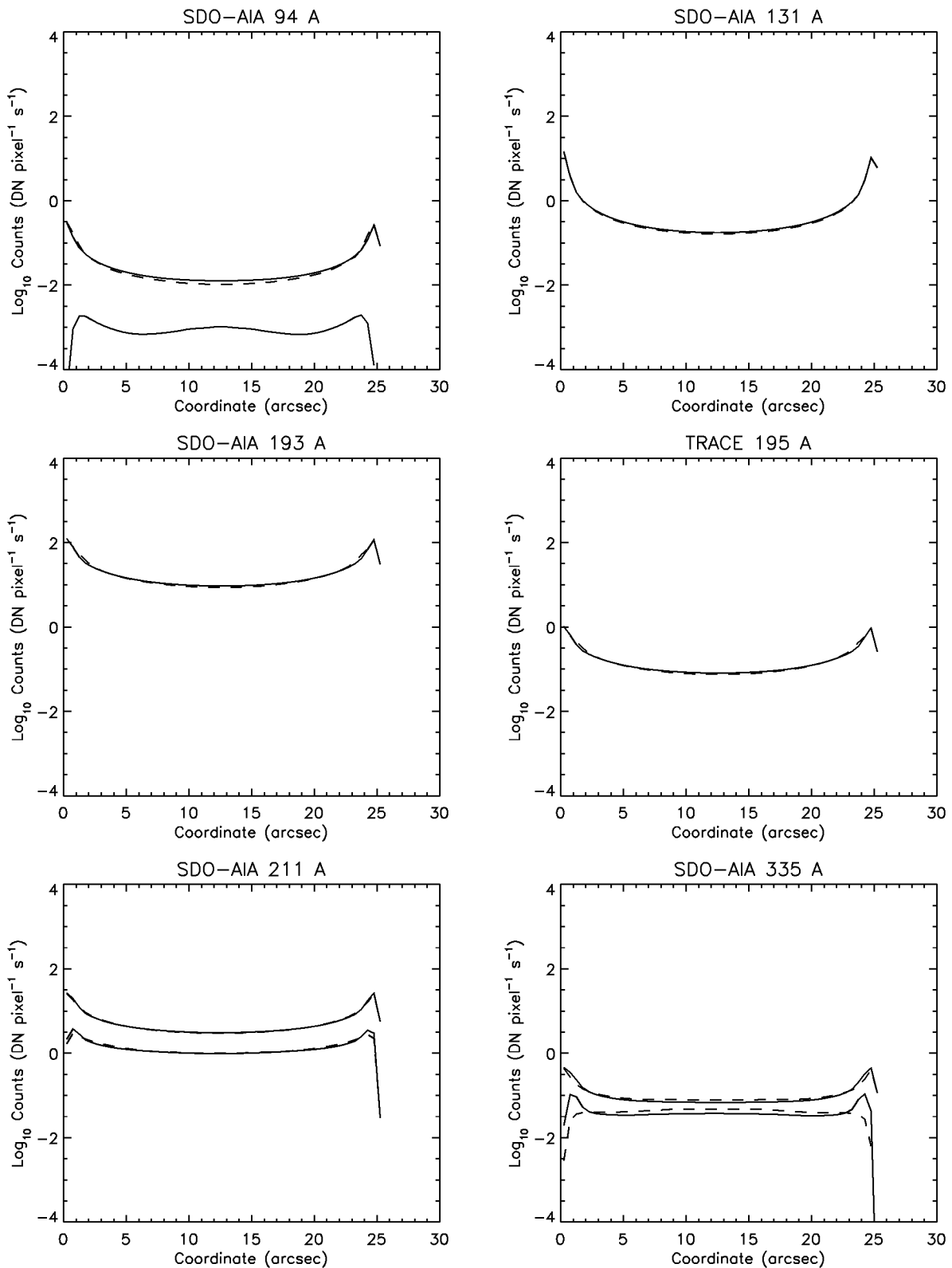


Fig. 3.— Synthesised total emission (upper pair of curves in each panel) and hot emission only (lower pair of curves in each panel) along the multi-stranded loop corresponding to Run 3 in a selection of SDO-AIA channels and the TRACE 195 Å channel. Solid lines denote equilibrium ionization and dashed lines nonequilibrium.

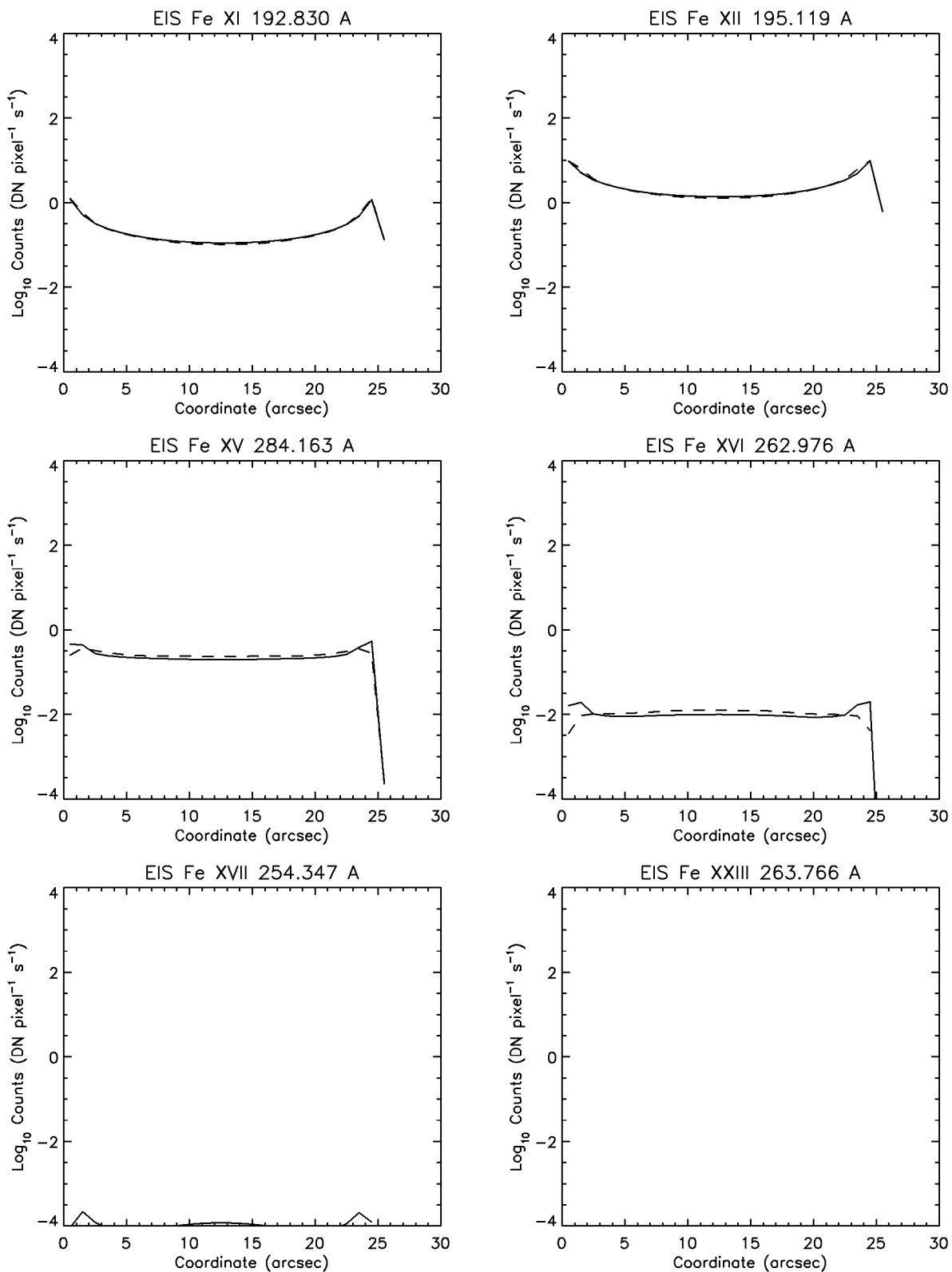


Fig. 4.— Synthesised emission along the multi-stranded loop corresponding to Run 3 for a selection of spectral lines formed at different temperatures as would be observed by Hinode-EIS. Solid lines denote equilibrium ionization and dashed lines nonequilibrium.

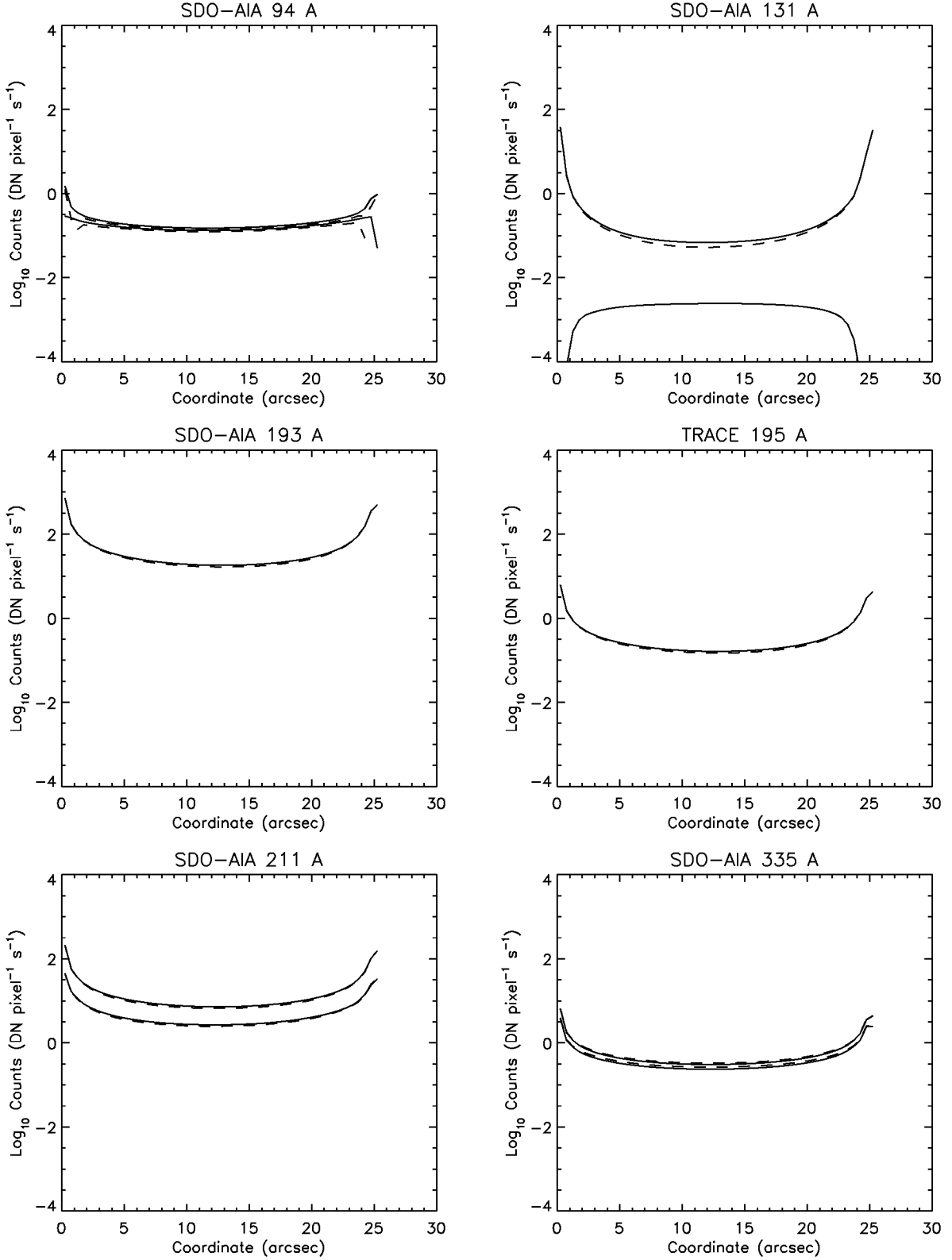


Fig. 5.— Synthesised total emission (upper pair of curves in each panel) and hot emission only (lower pair of curves in each panel) along the multi-stranded loop corresponding to Run 5 in a selection of SDO-AIA channels and the TRACE 195 Å channel. Solid lines denote equilibrium ionization and dashed lines nonequilibrium.

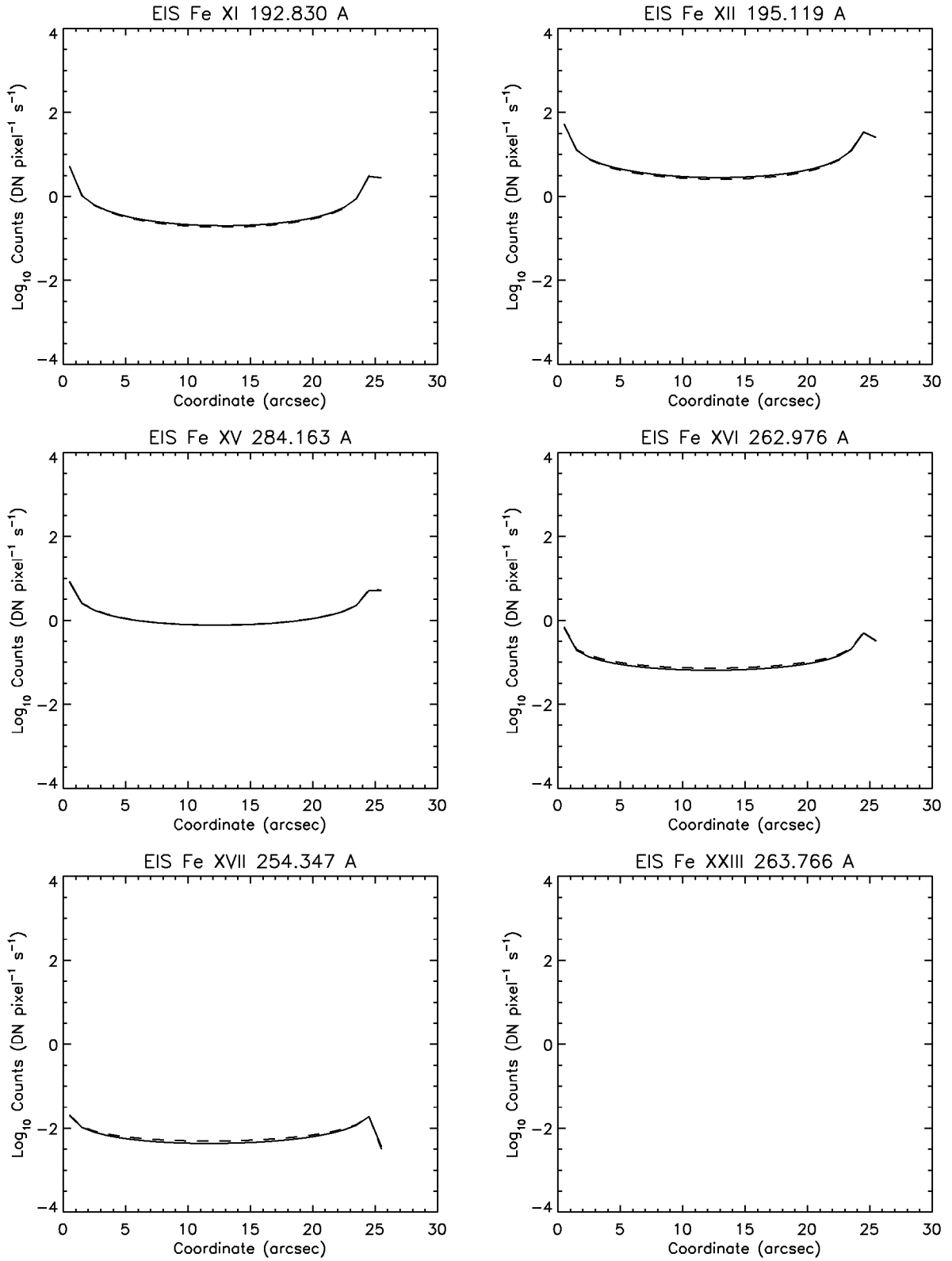


Fig. 6.— Synthesised emission along the multi-stranded loop corresponding to Run 5 for a selection of spectral lines formed at different temperatures as would be observed by Hinode-EIS. Solid lines denote equilibrium ionization and dashed lines nonequilibrium.

slower to equilibrate.

Some readers may question an initial density as high as 10^9 cm^{-3} . If nanoflares are the dominant source of heating in the corona, then any steady background heating that exists must be at a low level and certainly would not produce an initial static equilibrium with such a large density. However, the frequency with which nanoflares repeat on each strand is not known, and it is possible that a new nanoflare occurs before the plasma from the previous cycle has fully drained. Our simulations with high initial density are meant to approximate this situation. Note that the temperature of the initial atmosphere plays essentially no role.

4.2. Long loops

In this section we discuss our results for loops of greater length, $2L = 80 \text{ Mm}$. The increased length leads to longer cooling times (Bradshaw and Cargill 2010) and so our numerical experiments are allowed to evolve for 3000 s in the cases described in this section. This means that the loop is now composed of 3001 individual strands, with a cross sectional area that is one-third that of the short loop strands. The diameter of the composite loop is still approximately equivalent to an AIA pixel.

Runs 9-12 (Table 1) are the longer equivalents of Runs 2-5, following the evolution of a strand of initial coronal density 10^8 cm^{-3} subject to volumetric heating at a rate of $0.1 \text{ erg cm}^{-3} \text{ s}^{-1}$ for $t_H = 10, 30, 100$, and 300 s . The apex density and ion temperature at the conclusion of heating in Runs 9 and 10 barely change from their initial values, while the electron temperature rises to 10 MK. The apex temperature reached is about twice that of the equivalent Runs 2 and 3, despite the equal amount of energy released per particle, because the longer loop gives rise to a weaker foot-point to apex temperature gradient and thermal conduction is consequently less effective at removing the excess energy from the corona. Runs 11 and 12 see an order of magnitude increase

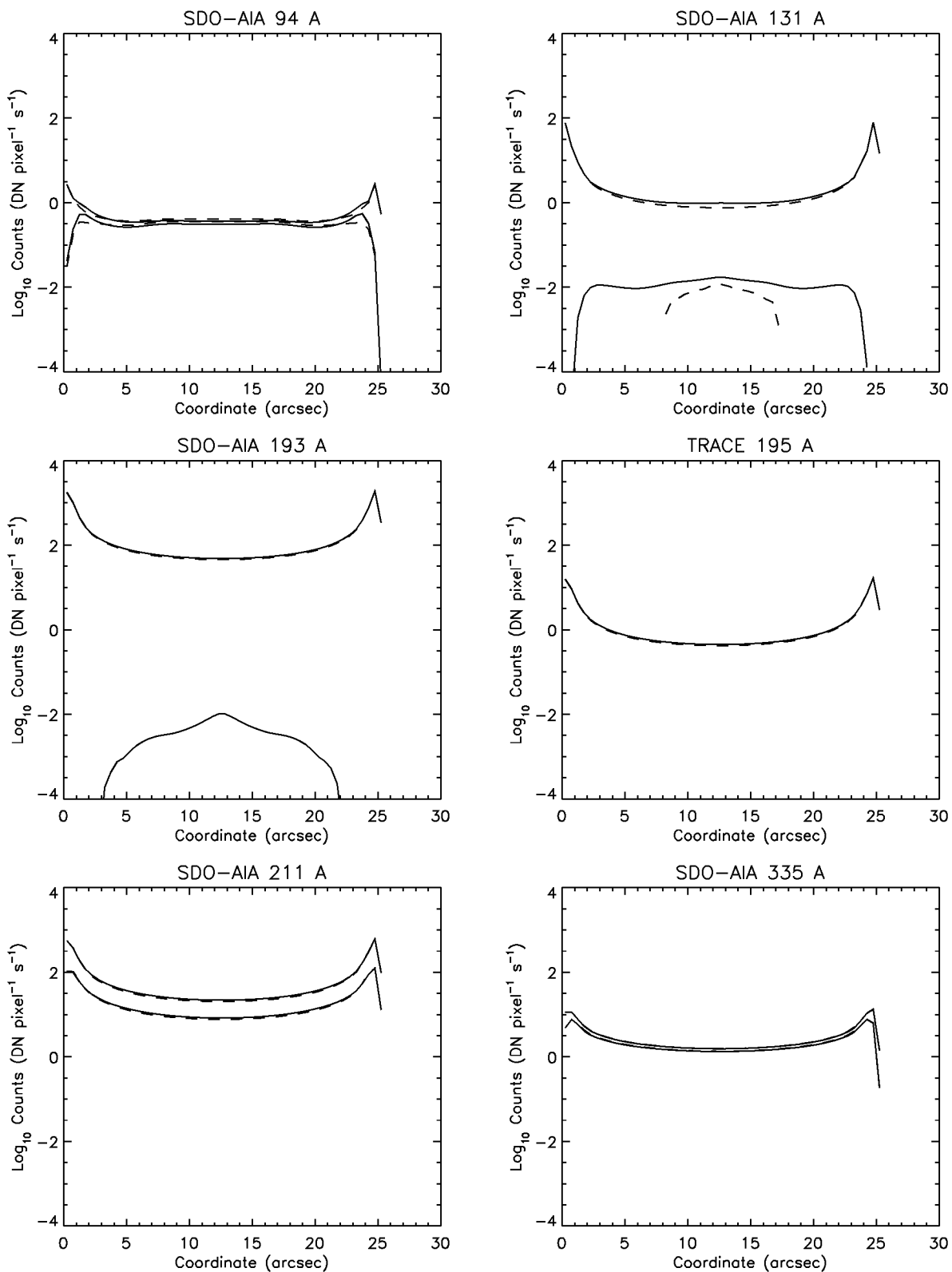


Fig. 7.— Synthesised total emission (upper pair of curves in each panel) and hot emission only (lower pair of curves in each panel) along the multi-stranded loop corresponding to Run 7 in a selection of SDO-AIA channels and the TRACE 195 Å channel. Solid lines denote equilibrium ionization and dashed lines nonequilibrium.

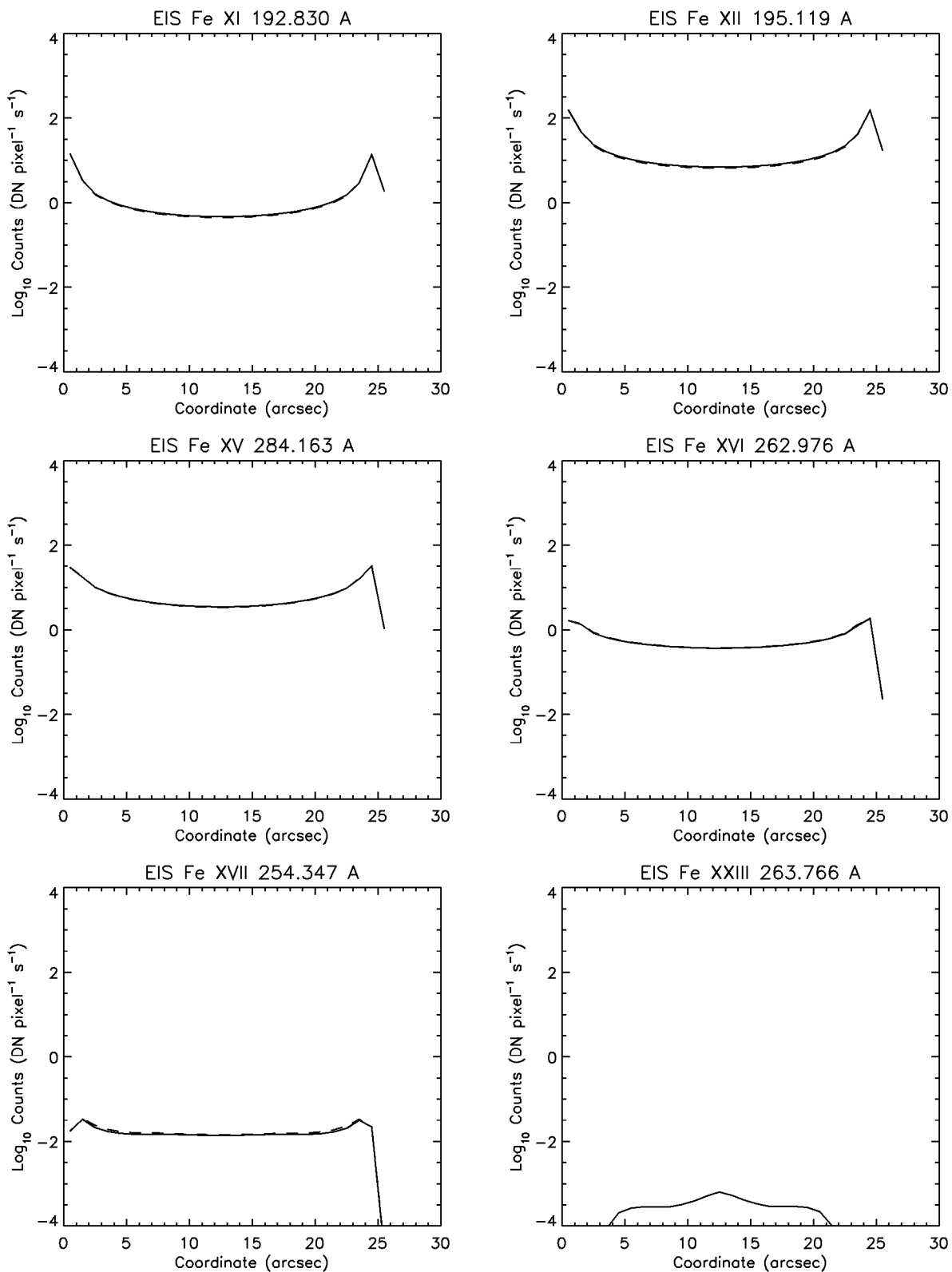


Fig. 8.— Synthesised emission along the multi-stranded loop corresponding to Run 7 for a selection of spectral lines formed at different temperatures as would be observed by Hinode-EIS. Solid lines denote equilibrium ionization and dashed lines nonequilibrium.

in the apex density at the end of heating and ion temperatures that actually exceed the electron temperatures. This is due to interacting waves which preferentially heat the ions by compressive effects.

Figures 9 and 10 show the total emission along the loop constructed from the results of Run 10 for SDO-AIA, TRACE and Hinode-EIS. Figures 11 and 12 show the results for Run 12. The corresponding figures for Runs 9 and 11 are provided in the online material. The hot components of the emission are less than or much less than half of the total emission in all of the AIA channels for Run 10, except for the 335 Å channel that has a strong contribution from Fe XVI. Where a contribution from the hot ions can be seen in the figures the emission is close to equilibrium, though departures are evident towards the loop foot-points for Fe XVIII in the 94 Å channel which can also be seen in the EIS Fe XVII line. For Run 12 the hot emission dominates the AIA 94 and 335 Å channels, with a strong foot-point component in the 211 Å channel. The equilibrium calculation predicts a weak component of Fe XXIV emission above the threshold in the 193 / 195 Å channels and from the EIS Fe XXIII line, but this is absent from the nonequilibrium calculation.

The detectable emission for the initial conditions and heating scenarios explored in Runs 9-12 are not representative of the temperatures attained. The peak electron temperatures are above 10 MK, whereas the figures show the hottest detectable emission is from the Fe XVIII population which peaks near 6 MK in equilibrium.

Runs 13 and 14 (Table 1) are the longer equivalents of Runs 7 and 8, following the evolution of a strand of initial coronal density 10^9 cm^{-3} subject to volumetric heating at a rate of $1.0 \text{ erg cm}^{-3} \text{ s}^{-1}$ for $t_H = 10$ and 30 s. The apex density at the conclusion of heating in both runs is actually lower than the initial density and this is because the pressure gradient that develops in the corona during heating becomes sufficiently strong that significant material can be forced from the apex region of the loop before it can be refilled. The pressure is allowed to build to such

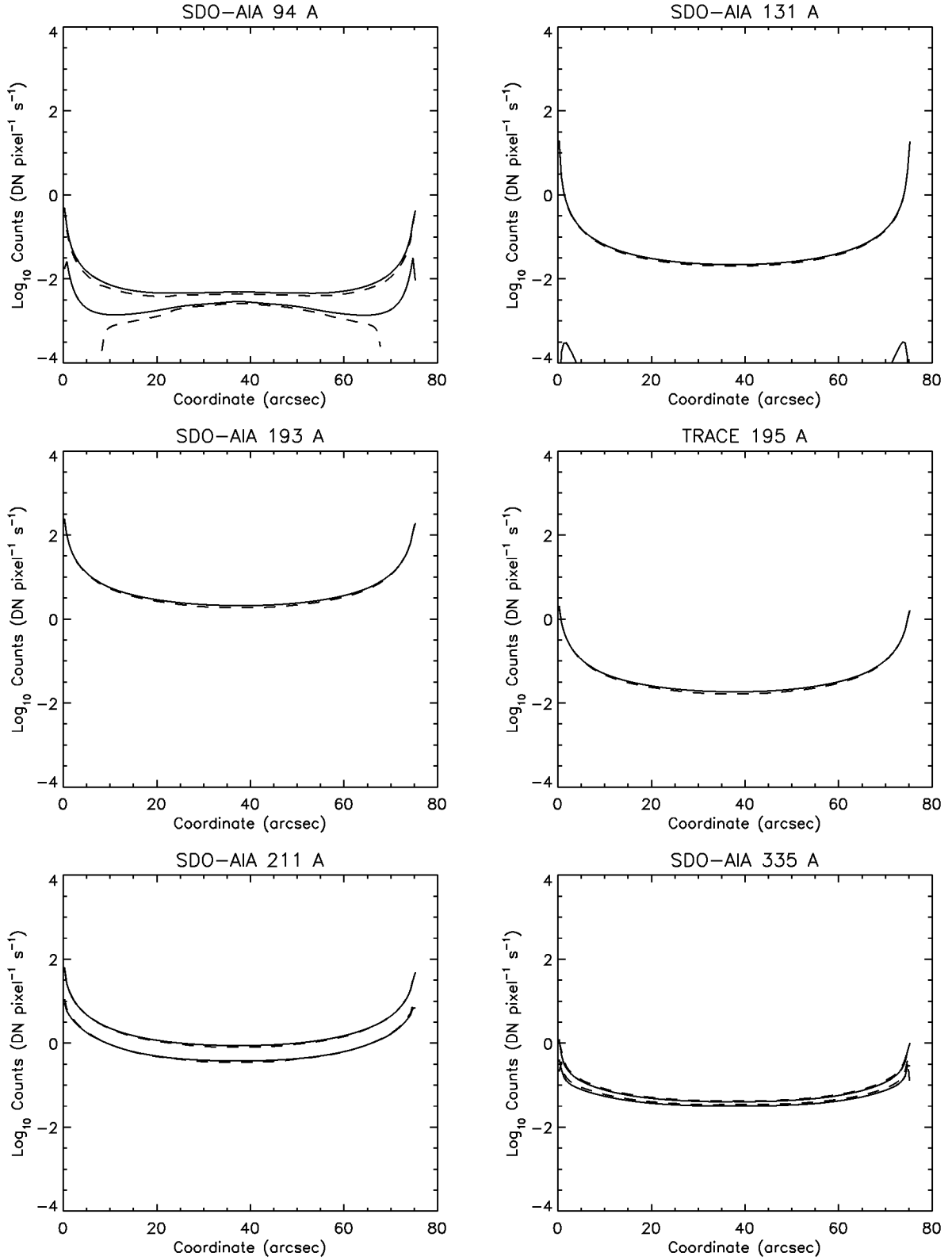


Fig. 9.— Synthesised total emission (upper pair of curves in each panel) and hot emission only (lower pair of curves in each panel) along the multi-stranded loop corresponding to Run 10 in a selection of SDO-AIA channels and the TRACE 195 Å channel. Solid lines denote equilibrium ionization and dashed lines nonequilibrium.

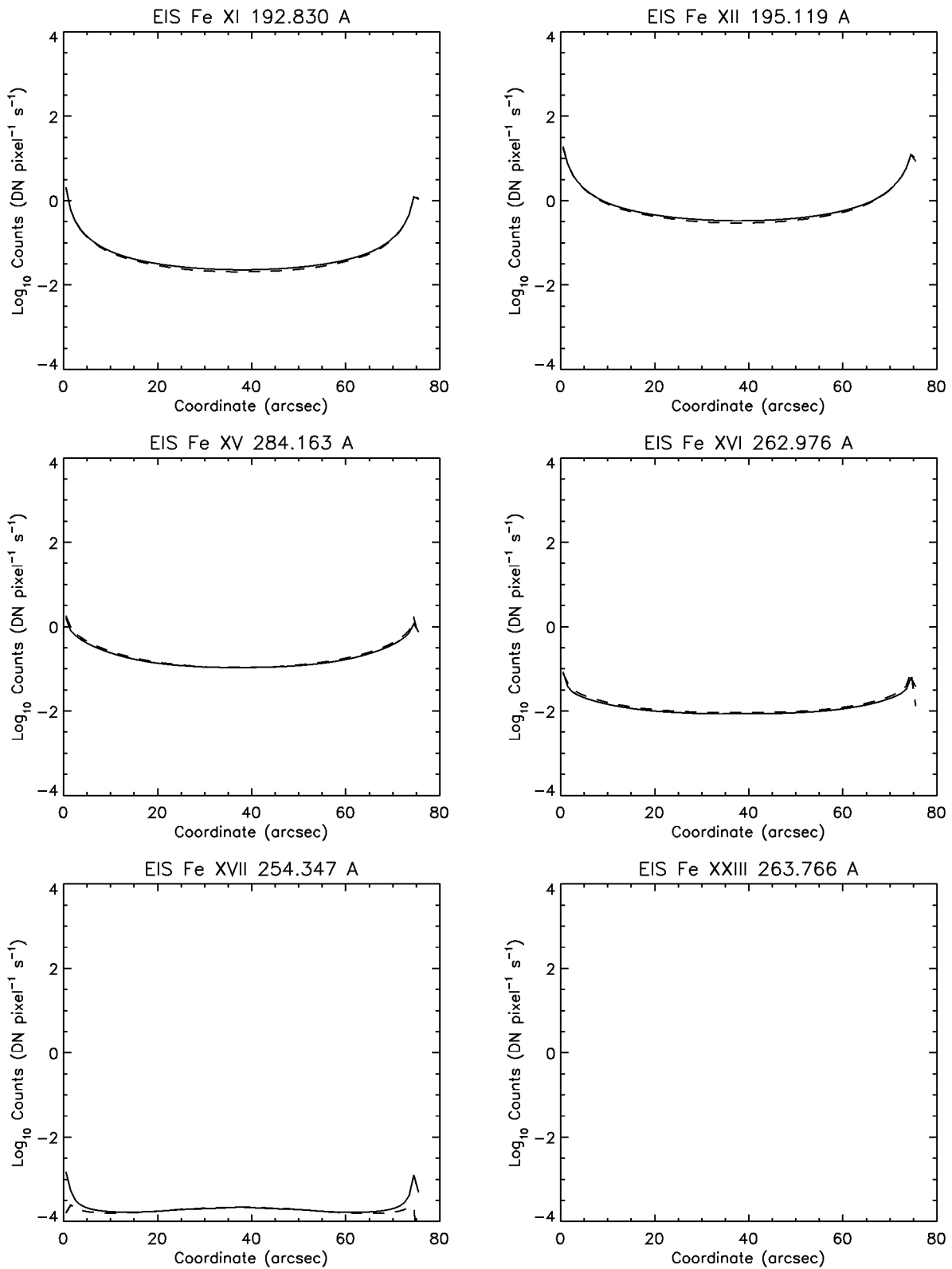


Fig. 10.— Synthesised emission along the multi-stranded loop corresponding to Run 10 for a selection of spectral lines formed at different temperatures as would be observed by Hinode-EIS. Solid lines denote equilibrium ionization and dashed lines nonequilibrium.

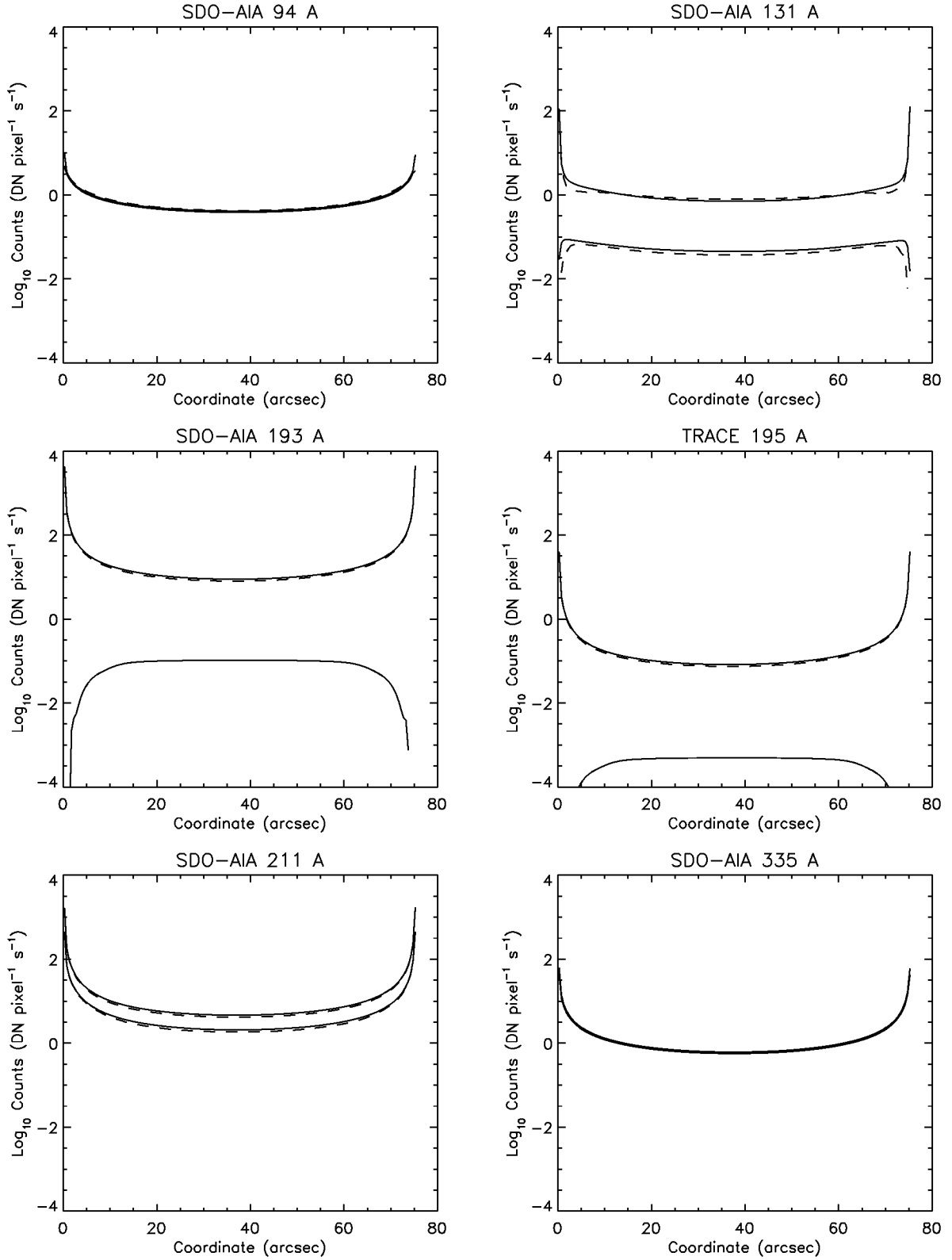


Fig. 11.— Synthesised total emission (upper pair of curves in each panel) and hot emission only (lower pair of curves in each panel) along the multi-stranded loop corresponding to Run 12 in a selection of SDO-AIA channels and the TRACE 195 Å channel. Solid lines denote equilibrium ionization and dashed lines nonequilibrium.

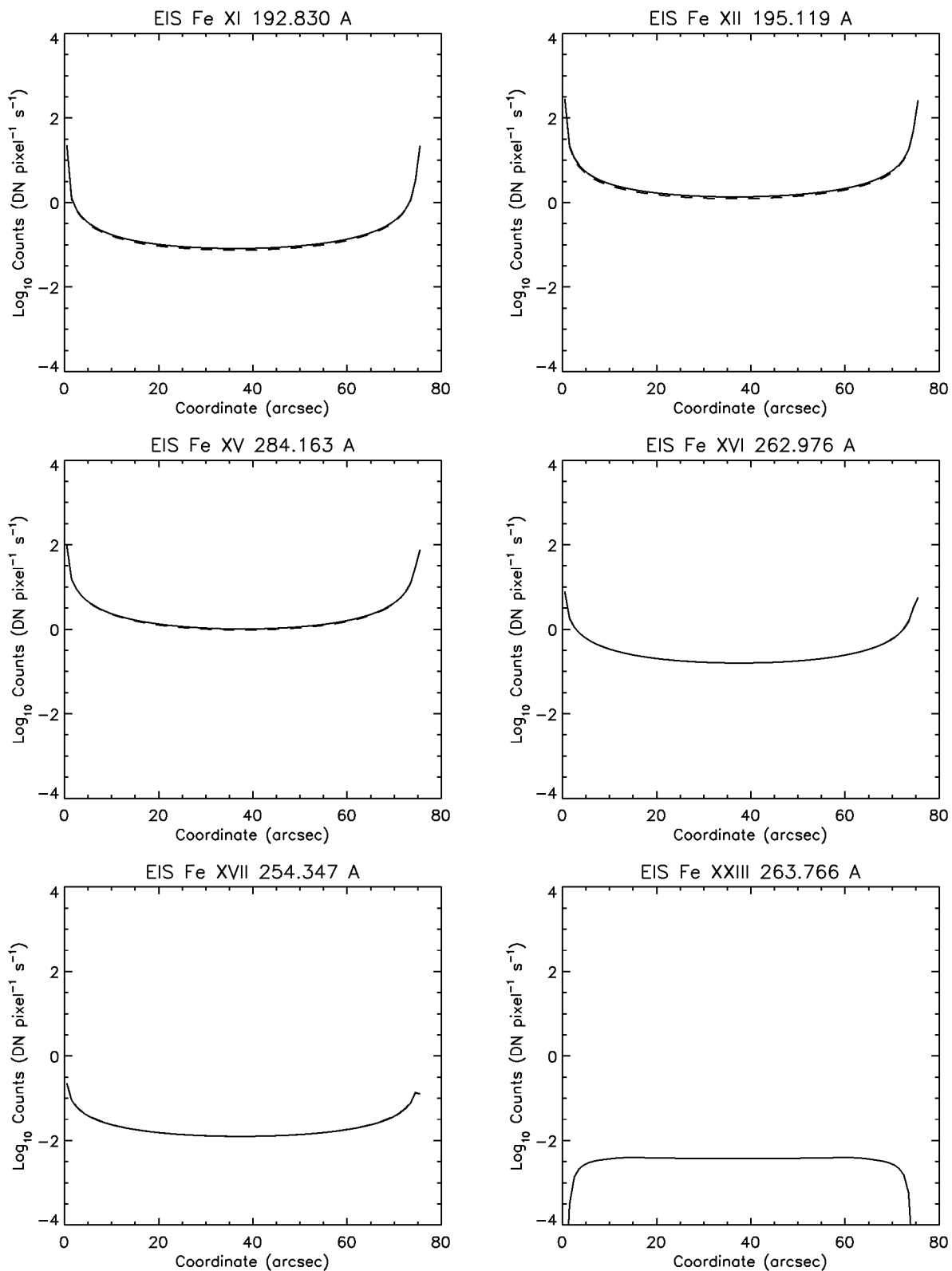


Fig. 12.— Synthesised emission along the multi-stranded loop corresponding to Run 12 for a selection of spectral lines formed at different temperatures as would be observed by Hinode-EIS. Solid lines denote equilibrium ionization and dashed lines nonequilibrium.

extremes in these cases, again despite an equal release of energy per particle to Runs 9-12, due to the twin factors of the increased loop length and greater initial density hampering the ability of thermal conduction to remove the excess energy from the corona. The electron temperature is thus able to reach 20 MK in both runs with a commensurately strong pressure enhancement. The ion temperature, as may be expected in this case, increases only slightly relative to the change in the electron temperature.

Figures 13 and 14 show the total emission along the loop constructed from the results of Run 14 for SDO-AIA, TRACE and Hinode-EIS. The corresponding figures for Run 13 are available online for comparison.

Similarly to Run 12, the hot emission dominates in the AIA 94 and 335 Å channels for Run 14 and is in equilibrium everywhere along the loop. This is also largely true for Run 13 ($\tau_H = 10$ s) and arises despite the lower coronal density, compared with the equivalent short loop runs, because the increased cooling time gives the ion populations more time to equilibrate. The equilibrium calculation grossly overestimates the contribution from Fe XXIV in the 193 / 195 Å channels and so we do not expect to observe emission characteristic of the 20 MK temperatures attained. The 211 Å channel remains contaminated by the many nearby emission lines swamping the Fe XIV line to which it is tuned, but our results do show that the 94 and 335 Å channels are clean. When EIS detects strong Fe XVI and XVII emission then the dominant components of the 335 and 94 Å channels should be the Fe XVI and XVIII lines to which they are respectively tuned. The enhanced sensitivity, and spatial and temporal resolution of AIA should then provide greater details concerning phenomena of interest at 2-6 MK. Assuming conditions similar to those we have explored, our results also show that strong emission in these channels is close to equilibrium, which means that techniques such as the emission measure loci method for determining temperatures can provide reliable estimates.

The 94 and 335 Å channels are sensitive within the temperature range of the hard-to-explain

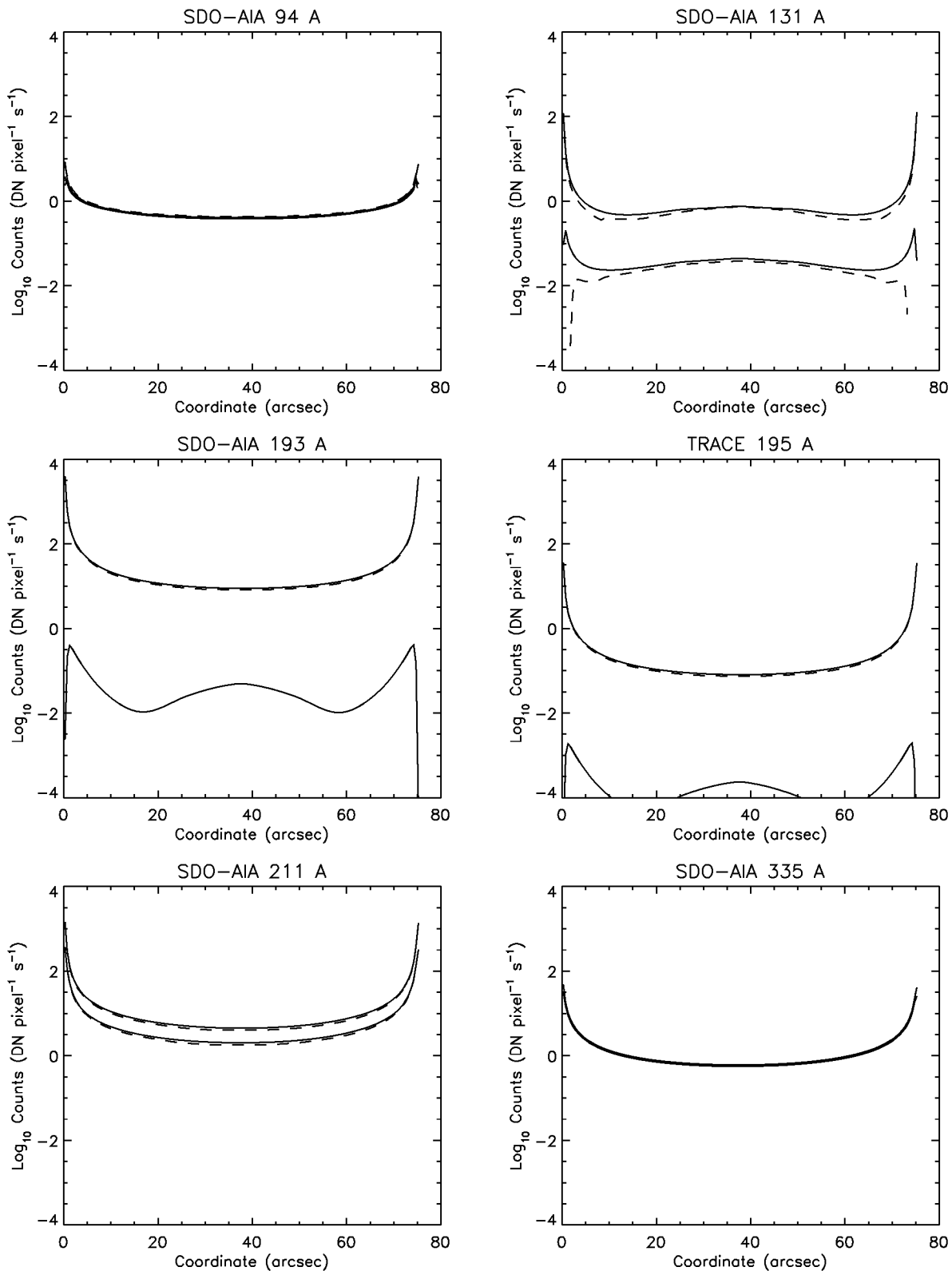


Fig. 13.— Synthesised total emission (upper pair of curves in each panel) and hot emission only (lower pair of curves in each panel) along the multi-stranded loop corresponding to Run 14 in a selection of SDO-AIA channels and the TRACE 195 Å channel. Solid lines denote equilibrium ionization and dashed lines nonequilibrium.

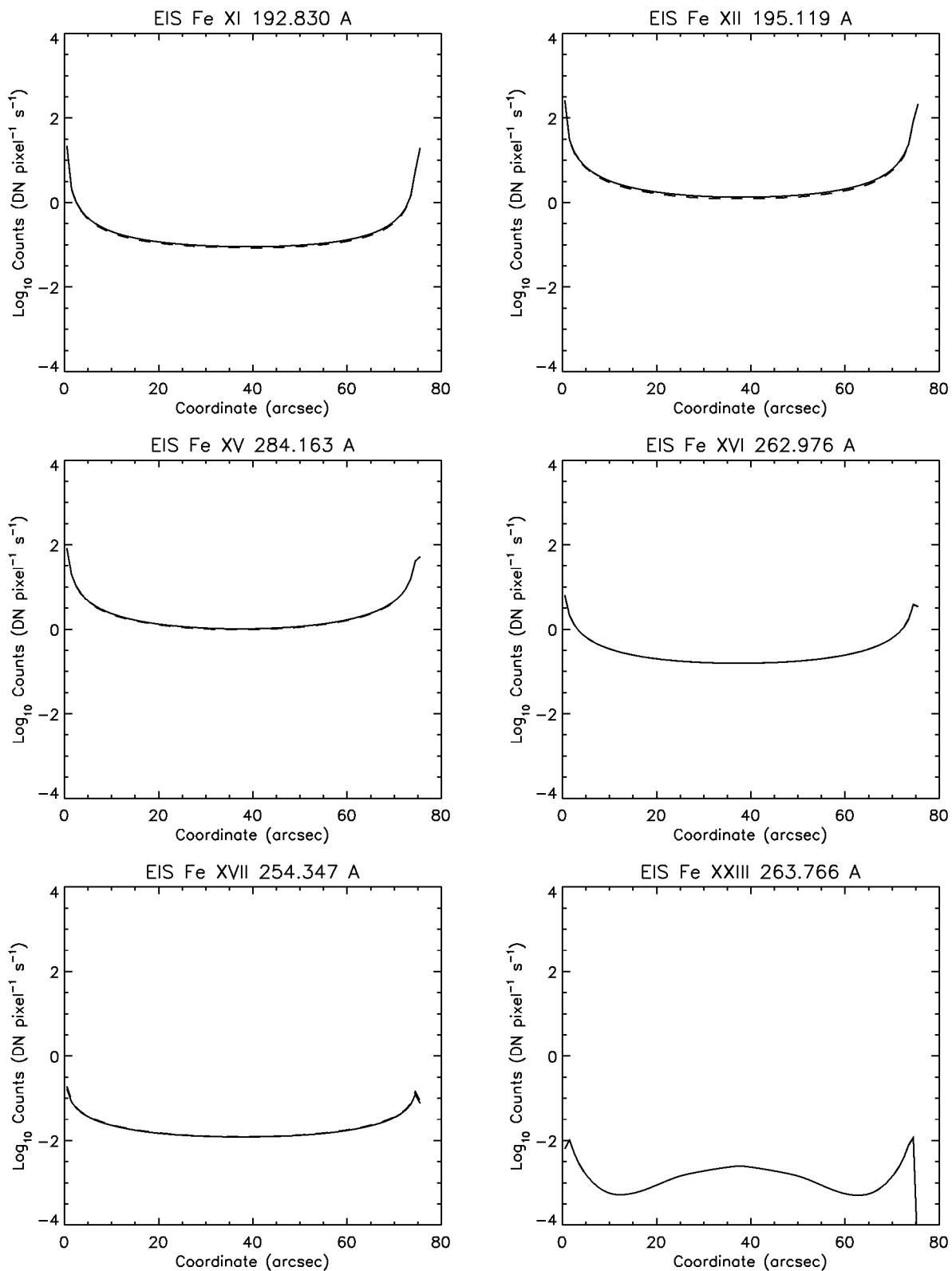


Fig. 14.— Synthesised emission along the multi-stranded loop corresponding to Run 14 for a selection of spectral lines formed at different temperatures as would be observed by Hinode-EIS. Solid lines denote equilibrium ionization and dashed lines nonequilibrium.

3-5 MK, hot and diffuse loops present in the cores of active regions. The cases of impulsive heating, on short and long time scales, of relatively tenuous and moderately dense loops, can all explain this emission according to our forward modeling results and perhaps this is why: (a) it is ubiquitous in these regions; and (b) it has been so difficult to determine whether such loops are impulsively or steadily heated. We are led to conclude from our investigations that it is difficult *not* to create loops that appear bright in the 193 / 195 Å (1.5 MK), and 94 and 335 Å (2-6 MK) ranges.

We are also able to place an upper limit on the temperature of the emission that we may expect to observe with these instruments. Our nonequilibrium calculations demonstrate that we should not expect to observe any Fe XXIII or XXIV emission and therefore any detectable emission must be formed below the Fe XXIII formation temperature of about 16 MK. This limit can be further refined by noting that the hot component of the emission in the AIA 131 Å channel is then most likely due to Fe XX and which is not a dominant component of the total observed emission, but may not be negligible either. Chianti predicts a total of 2602 Fe XX emission lines falling within a 40 Å window centred on 131 Å, which suggests a reasonable chance that a number of particularly strong lines may be present within that range and amenable to detection by a sufficiently sensitive spectrometer. The observational evidence provided by Reale et al. (2009a,b), Schmelz et al. (2009b), McTiernan (2009) and Sylwester et al. (2010) of faint emission at 10 MK, the formation temperature of Fe XX, suggests that this could be an avenue worth pursuing in the future.

5. Summary and conclusions

Our study has two main goals: 1. Determine the degree to which ionization nonequilibrium suppresses the intensity of hot emissions produced by impulsively heated plasmas. (To what extent does the high-temperature DEM inferred from observations by assuming ionization equilibrium

underestimate the true DEM of the plasma?) 2. Determine, within the framework of unresolved nanoflare-heated strands, which temperature plasma dominates the signal detected in different AIA channels. (Are the channels that are nominally thought of as hot (94, 131 Å) actually observing hot plasma?)

We have addressed these goals by performing a series of hydrodynamic simulations. Because the true nature of coronal heating is not yet known, we have considered a variety of different circumstances. We varied both the properties of the nanoflare (magnitude and lifetime) and the properties of the initial strand atmosphere. We assumed that the initial atmosphere is a static equilibrium maintained by a steady background heating. However, because the response to the nanoflare is largely independent of the initial temperature, our simulations are also relevant to the situation of no background heating, with a new nanoflare occurring after the strand has drained to the assumed density (Table 1, column 3).

Deviations from ionization equilibrium are greatest when the density is low, the temperature is high, and conditions are changing rapidly. A crude proxy for the magnitude of the effect is the difference in electron and ion kinetic temperatures at the end of heating (Table 1, last 2 columns). This is another form of nonequilibrium. It is important to realize that these two types of nonequilibrium are not directly related and do not affect each other. Our ionization results would be essentially unchanged if the electron and ion temperatures were forced to be equal (i.e., a single fluid approximation).

We find that the most important parameter in our simulations is the nanoflare duration. As can be seen by comparing cases where only t_H differs (e.g., Runs 2-5 and 9-12), the shorter duration nanoflares do not allow enough time for the electron and ion temperatures to equilibrate before cooling begins. More importantly, the ionization temperature lags well below its equilibrium value (the electron temperature), and by the time it catches up, the electron temperature has decreased dramatically. High ionization stages are only very weakly populated as a result. This

is reflected in Table 11, which gives the ratio of the nonequilibrium intensity to the equilibrium intensity for 6 well-known spectral lines. The lines are listed in order of increasing temperature (in equilibrium). Values in parentheses are from the loop apex. Again comparing Runs 2-5 and 9-12, we see that the intensity ratios of the hot lines are very small for 10 s nanoflares, meaning far from equilibrium, and they increase to near unity for 300 s nanoflares. Cooler lines are almost always near equilibrium because they are formed well after the nanoflare has ended, when the plasma is evolving much more slowly.

Runs 8 and 13 are exceptions to the rule. Despite a short nanoflare, the hot line intensities are near equilibrium because the initial density of 10^9 cm^{-3} is very high. The effect of the initial density is significant and can be seen throughout Table 11. Deviations from equilibrium get progressively smaller as the initial density increases from 10^7 to 10^8 to 10^9 cm^{-3} in Runs 1, 2, and 6, which had identical nanoflare duration. The same ordering is clearly present for the other low/high density pairs (3/7, 9/13, 10/14).

Our simulations allow us to make the following general statements. Deviations from ionization equilibrium can be severe and emission line intensities can be greatly suppressed. Hotter lines are more affected because they are formed in the early stages of cooling when the temperature is decreasing most rapidly. The deviations are more pronounced for shorter duration nanoflares and lower initial densities. Attempts to infer a high-temperature emission measure from observed line intensities may greatly underestimate the true emission measure if ionization equilibrium is assumed.

We now compare some predicted and observed line intensities. Table 9 gives the EIS count rates that would be expected at the apex of a loop bundle having a diameter of 380 km (0.5"). Since most of the emission from active regions comes from a diffuse component rather than observationally distinct loops, we instead imagine a space filling collection of unresolved strands having a total line-of-sight thickness of $2 \times 10^4 \text{ km}$. To predict the intensity for this situation, we

must multiply the count rates in the table by a factor of 134.

The volume element of the strand bundle observable in a single EIS pixel is given by

$$V_{bundle} = \pi \left(\frac{d}{2} \right)^2 2d, \quad (10)$$

where d is the dimension of an SDO-AIA pixel and so $2d$ is the dimension of an EIS pixel. The volume element of the diffuse corona observable in a single EIS pixel is given by

$$V_{diffuse} = 2d \times 2d \times L, \quad (11)$$

where L is the line-of-sight depth through the diffuse corona. The ratio of these two quantities is then

$$R = \frac{V_{diffuse}}{V_{bundle}} = \frac{8L}{\pi d}. \quad (12)$$

Substituting the appropriate numerical values gives

$$R = \frac{8 \times 2 \times 10^4}{\pi \times 380} = 134. \quad (13)$$

Note that it has been assumed that the nanoflares repeat on each strand once every 1000 or 3000 s for the short and long loops, respectively. If the delay times are different, the predicted count rates must be changed accordingly.

The count rates in Table 9 cover a wide range of values in each line, especially the hottest lines, where the spread can reach several orders of magnitude. The median intensities for nonequilibrium ionization, adjusted by the factor of 134, are 4, 0.3, and 8 DN pixel⁻¹ s⁻¹ for Ca XVII (192.86), Fe XVII (254.87), and Fe XVI (262.98), respectively. In comparison, H. P. Warren

(2010, private communication) reports count rates of 42, 2, and 108 DN pixel⁻¹ s⁻¹ for spatially averaged observations of the core of NOAA active region 10960 observed on 2007 June 5 (bright area in the Ca XVII image of Fig. 2 in Warren et al. (2010)). The Fe XV (284.16) emission in most of our models is about 10 times brighter than the Ca XVII emission, which agrees with the observed ratio of 8.7. We conclude that observations are consistent with at least some of our nanoflare models.

We now turn to AIA and the issue of what plasma dominates the signal that is detected in the different channels. The channels were chosen to have different temperature sensitivities, so the thermal properties of the observed plasma could be diagnosed. However, each channel has some sensitivity to all temperatures, and this can be a significant source of ambiguity. This is especially true of the 94 and 131 Å channels, with temperature response functions that are doubly peaked. These are sometime referred to as hot channels, because one of the two peaks is at high temperatures. What happens if the observed plasma emits far more strongly at warm temperatures than at hot temperatures? This is precisely the situation we expect for unresolved nanoflare strands. There is far less material at high temperatures because newly heated strands cool rapidly before evaporation has a chance to increase the density. On top of this, ionization nonequilibrium suppressed the hot emission much more than it does the warm emission. As a consequence, the measured signal comes primarily from warm plasma in most cases. The very hottest plasma is a minor or negligible contributor.

This is clearly demonstrated in Table 8, which gives the ratio of the contributions to the signal from hot lines and all lines in each of the channels. The ratio is small for those runs in which the initial density is low and the heating fast. It is extremely small for the two channels (131 and 193 Å) sensitive to the hottest emission (Fe XX to XXIV) regardless of the initial density and heating period. However, it can be large for higher densities and / or longer heating periods for the 94 and 335 Å channels, which are sensitive to emission in the 2 to 6 MK range

(Fe XVI to XVIII). This is the temperature range of the hard-to-explain, diffuse active region emission. Our forward modeling results show that it is rather difficult not to create plasma that emits strongly within the region of 1.5 MK and in the range 2 to 5 MK, across a broad range of nanoflare-type scenarios, which are representative of the most commonly observed coronal loops. The cooler emission arises from unresolved strands cooling through the formation temperature of the particularly strong Fe XII line. The hotter emission arises from unresolved strands cooling through the formation temperatures of strong Fe XV to XVIII lines. We therefore conclude that the combined effects of nanoflare-type heating and a nonequilibrium ionization state lead to predictions for observable quantities that are entirely consistent with what is actually observed.

We thank Peter Cargill and Harry Warren for helpful discussions. We also thank Harry for providing the EIS count rates discussed in Section 5 and Mark Weber for providing the SDO-AIA wavelength resolved response functions. This work was supported by the NASA Supporting Research and Technology program.

A. SDO-AIA channel intensity tables

B. Hinode-EIS emission line intensity tables

Table 3: Intensities ($\text{DN pixel}^{-1} \text{ s}^{-1}$) at the loop apex in a selection of SDO-AIA channels calculated for hot ions only. Values calculated for nonequilibrium ionization are given in brackets for each run.

#	94	131	193	211	335	TRACE 195
1	1.95×10^{-7} (0.00)	2.37×10^{-9} (0.00)	0.00 (0.00)	2.29×10^{-2} (0.00)	1.09×10^{-5} (0.00)	0.00 (0.00)
2	5.66×10^{-6} (0.00)	2.77×10^{-8} (0.00)	0.00 (0.00)	1.61×10^{-1} (1.55×10^{-1})	2.28×10^{-3} (0.00)	0.00 (0.00)
3	1.04×10^{-3} (0.00)	3.71×10^{-7} (0.00)	0.00 (0.00)	9.81×10^{-1} (1.01×10^0)	3.74×10^{-2} (4.77×10^{-2})	0.00 (0.00)
4	4.11×10^{-2} (3.63×10^{-2})	4.92×10^{-4} (0.00)	0.00 (0.00)	3.28×10^0 (2.93×10^0)	2.67×10^{-1} (3×10^{-1})	0.00 (0.00)
5	1.33×10^{-1} (1.24×10^{-1})	2.43×10^{-3} (0.00)	0.00 (0.00)	2.69×10^0 (2.49×10^0)	2.37×10^{-1} (2.66×10^{-1})	0.00 (0.00)
6	2.58×10^{-2} (2.31×10^{-2})	2.06×10^{-4} (0.00)	1×10^{-4} (0.00)	3.72×10^0 (3.58×10^0)	2.63×10^{-1} (2.83×10^{-1})	4.77×10^{-7} (0.00)
7	3.09×10^{-1} (3.55×10^{-1})	1.73×10^{-2} (1.15×10^{-2})	1.05×10^{-2} (0.00)	8.29×10^0 (7.69×10^0)	1.33×10^0 (1.35×10^0)	4.98×10^{-5} (0.00)
8	6.94×10^{-1} (7.56×10^{-1})	3.3×10^{-2} (2.01×10^{-2})	5.16×10^{-3} (0.00)	1.02×10^1 (9.72×10^0)	2.02×10^0 (2.05×10^0)	2.45×10^{-5} (0.00)
9	1.05×10^{-4} (0.00)	9.81×10^{-7} (0.00)	2.5×10^{-6} (0.00)	1.2×10^{-1} (1.42×10^{-1})	5.62×10^{-3} (6.65×10^{-3})	1.19×10^{-8} (0.00)
10	2.88×10^{-3} (2.59×10^{-3})	3.61×10^{-6} (0.00)	1.07×10^{-5} (0.00)	3.76×10^{-1} (3.53×10^{-1})	3.19×10^{-2} (3.46×10^{-2})	5.07×10^{-8} (0.00)
11	6.19×10^{-2} (6.96×10^{-2})	2.45×10^{-3} (1.26×10^{-3})	1.85×10^{-3} (0.00)	1.08×10^0 (8.99×10^{-1})	1.89×10^{-1} (1.94×10^{-1})	8.8×10^{-6} (0.00)
12	3.84×10^{-1} (3.96×10^{-1})	4.54×10^{-2} (3.7×10^{-2})	1.04×10^{-1} (0.00)	2.07×10^0 (1.84×10^0)	5.65×10^{-1} (5.67×10^{-1})	4.96×10^{-4} (0.00)
13	6.19×10^{-1} (6.43×10^{-2})	1.91×10^{-3} (1.07×10^{-3})	8.8×10^{-4} (0.00)	1.11×10^0 (9.66×10^{-1})	1.77×10^{-1} (1.82×10^{-1})	4.19×10^{-6} (0.00)
14	3.86×10^{-1} (4.04×10^{-1})	4.44×10^{-2} (3.81×10^{-2})	4.93×10^{-2} (0.00)	2.02×10^0 (1.79×10^0)	5.58×10^{-1} (5.6×10^{-1})	2.35×10^{-4} (0.00)

Table 4: Integrated intensities (DN s^{-1}) along the loop in a selection of SDO-AIA channels calculated for hot ions only.

#	94	131	193	211	335	TRACE 195
1	2.65×10^{-4} (0.00)	1.06×10^{-7} (0.00)	0.00 (0.00)	1.32×10^0 (0.00)	2.87×10^{-2} (0.00)	0.00 (0.00)
2	1.23×10^{-3} (0.00)	6.66×10^{-7} (0.00)	0.00 (0.00)	5.42×10^0 (2.69×10^0)	1.07×10^{-1} (0.00)	0.00 (0.00)
3	4.68×10^{-2} (0.00)	2.29×10^{-5} (0.00)	0.00 (0.00)	7.11×10^1 (7.04×10^1)	2.05×10^0 (2.04×10^0)	0.00 (0.00)
4	2.34×10^0 (1.79×10^0)	1.75×10^{-2} (0.00)	0.00 (0.00)	3.64×10^2 (3.48×10^2)	2.4×10^1 (2.57×10^1)	0.00 (0.00)
5	8.61×10^0 (6.8×10^0)	9.14×10^{-2} (0.00)	0.00 (0.00)	3.24×10^2 (3.15×10^2)	2.67×10^1 (2.87×10^1)	0.00 (0.00)
6	8.9×10^{-1} (3.79×10^{-1})	1.36×10^{-2} (0.00)	1.97×10^{-3} (0.00)	2.99×10^2 (2.95×10^2)	1.5×10^1 (1.62×10^1)	9.38×10^{-6} (0.00)
7	1.55×10^1 (1.57×10^1)	5.25×10^{-1} (1.39×10^{-1})	1.4×10^{-1} (0.00)	1.16×10^3 (1.13×10^3)	1.2×10^2 (1.23×10^2)	6.68×10^{-4} (0.00)
8	3.82×10^1 (3.17×10^1)	1.31×10^0 (2.78×10^{-1})	1.28×10^0 (0.00)	1.74×10^3 (1.72×10^3)	2.23×10^2 (2.29×10^2)	6.1×10^{-3} (0.00)
9	1.87×10^{-2} (0.00)	2.78×10^{-4} (0.00)	3.02×10^{-4} (0.00)	3.27×10^1 (3.72×10^1)	9.23×10^{-1} (9.08×10^{-1})	1.44×10^{-6} (0.00)
10	4.3×10^{-1} (1.98×10^{-1})	4.23×10^{-3} (0.00)	1.33×10^{-3} (0.00)	1.57×10^2 (1.65×10^2)	8.34×10^0 (9.03×10^0)	6.35×10^{-6} (0.00)
11	1.26×10^1 (1.28×10^1)	3.25×10^{-1} (9.05×10^{-2})	1.52×10^{-1} (0.00)	7.34×10^2 (7.12×10^2)	7.54×10^1 (7.7×10^1)	7.21×10^{-4} (0.00)
12	1.08×10^2 (1.12×10^2)	8.57×10^0 (6.87×10^0)	1.19×10^1 (0.00)	1.78×10^3 (1.74×10^3)	2.92×10^2 (2.94×10^2)	5.68×10^{-2} (0.00)
13	9.53×10^0 (8.66×10^0)	1.9×10^{-1} (4.43×10^{-2})	2.6×10^{-1} (0.00)	6.63×10^2 (6.34×10^2)	6.39×10^1 (6.6×10^1)	1.24×10^{-3} (0.00)
14	9.41×10^1 (9.95×10^1)	5.7×10^0 (3.59×10^0)	7.7×10^0 (0.00)	1.76×10^3 (1.7×10^3)	2.78×10^2 (2.81×10^2)	3.66×10^{-2} (0.00)

Table 5: Intensities (DN pixel⁻¹ s⁻¹) at the loop apex in a selection of SDO-AIA channels calculated for all ions that emit within their wavelength sensitivity ranges.

#	94	131	193	211	335	TRACE 195
1	1.79×10^{-3} (2.01×10^{-3})	4.42×10^{-2} (4.28×10^{-2})	8.41×10^{-1} (9.05×10^{-1})	1.67×10^{-1} (1.3×10^{-1})	2.29×10^{-3} (2.03×10^{-3})	6.74×10^{-3} (7.01×10^{-3})
2	4.41×10^{-3} (4.44×10^{-3})	9.08×10^{-2} (8.52×10^{-2})	2.42×10^0 (2.78×10^0)	6.3×10^{-1} (6.92×10^{-1})	9.71×10^{-3} (7.65×10^{-3})	1.99×10^{-2} (2.31×10^{-2})
3	1.27×10^{-2} (1.04×10^{-2})	1.75×10^{-1} (1.64×10^{-1})	9.35×10^0 (8.68×10^0)	3.07×10^0 (2.99×10^0)	6.85×10^{-2} (7.81×10^{-2})	8.1×10^{-2} (7.54×10^{-2})
4	6.43×10^{-2} (5.71×10^{-2})	3.03×10^{-1} (2.85×10^{-1})	2.16×10^1 (1.89×10^1)	8.78×10^0 (7.71×10^0)	3.54×10^{-1} (3.78×10^{-1})	1.93×10^{-1} (1.68×10^{-1})
5	1.52×10^{-1} (1.4×10^{-1})	6.88×10^{-2} (5.3×10^{-2})	1.82×10^1 (1.66×10^1)	7.21×10^0 (6.62×10^0)	3.06×10^{-1} (3.3×10^{-1})	1.63×10^{-1} (1.49×10^{-1})
6	5.38×10^{-2} (4.87×10^{-2})	4.73×10^{-1} (4.5×10^{-1})	2.53×10^1 (2.41×10^1)	1.03×10^1 (9.76×10^0)	3.65×10^{-1} (3.81×10^{-1})	2.27×10^{-1} (2.16×10^{-1})
7	3.65×10^{-1} (4.07×10^{-1})	9.86×10^{-1} (7.61×10^{-1})	4.82×10^1 (4.55×10^1)	2.19×10^1 (2.04×10^1)	1.55×10^0 (1.56×10^0)	4.48×10^{-1} (4.21×10^{-1})
8	7.69×10^{-1} (8.21×10^{-1})	1.29×10^0 (1.02×10^0)	5.85×10^1 (5.56×10^1)	2.71×10^1 (2.55×10^1)	2.29×10^0 (2.31×10^0)	5.48×10^{-1} (5.19×10^{-1})
9	1.19×10^{-3} (8.38×10^{-4})	8.67×10^{-3} (6.87×10^{-3})	9.39×10^{-1} (8.41×10^{-1})	3.17×10^{-1} (3.36×10^{-1})	8.73×10^{-3} (9.95×10^{-3})	8.09×10^{-3} (7.37×10^{-3})
10	4.97×10^{-3} (4.4×10^{-3})	2.19×10^{-2} (2.02×10^{-2})	2.08×10^0 (1.85×10^0)	8.74×10^{-1} (8.03×10^{-1})	4.05×10^{-2} (4.26×10^{-2})	1.85×10^{-2} (1.65×10^{-2})
11	6.78×10^{-2} (7.47×10^{-2})	8.32×10^{-2} (5.58×10^{-2})	4.97×10^0 (4.4×10^0)	2.4×10^0 (2.02×10^0)	2.13×10^{-1} (2.15×10^{-1})	4.52×10^{-2} (3.97×10^{-2})
12	4.1×10^{-1} (4.24×10^{-1})	7.1×10^{-1} (7.98×10^{-1})	8.91×10^0 (8.01×10^0)	4.63×10^0 (4.17×10^0)	6.13×10^{-1} (6.11×10^{-1})	8.25×10^{-2} (7.45×10^{-2})
13	6.8×10^{-2} (6.97×10^{-2})	6.35×10^{-2} (4.74×10^{-2})	5.05×10^0 (4.54×10^0)	2.47×10^0 (2.15×10^0)	2.01×10^{-1} (2.05×10^{-1})	4.61×10^{-2} (4.1×10^{-2})
14	4.15×10^{-1} (4.34×10^{-1})	7.54×10^{-1} (7.29×10^{-1})	8.86×10^0 (8.14×10^0)	4.49×10^0 (4.01×10^0)	6.06×10^{-1} (6.04×10^{-1})	8.09×10^{-2} (7.4×10^{-2})

Table 6: Integrated intensities (DN s^{-1}) along the loop in a selection of SDO-AIA channels calculated for all ions that emit within their wavelength sensitivity ranges.

#	94	131	193	211	335	TRACE 195
1	1.84×10^{-1} (2.33×10^{-1})	9.46×10^0 (1.16×10^1)	6.61×10^1 (5.77×10^1)	1.3×10^1 (8.82×10^0)	2.59×10^{-1} (2.03×10^{-1})	5.34×10^{-1} (4.54×10^{-1})
2	4.63×10^{-1} (5.19×10^{-1})	1.87×10^1 (1.87×10^1)	1.91×10^2 (2.03×10^2)	4.02×10^1 (3.58×10^1)	7.31×10^{-1} (6.05×10^{-1})	1.54×10^0 (1.6×10^0)
3	1.93×10^0 (1.96×10^0)	5.47×10^1 (5.44×10^1)	1.13×10^3 (1.15×10^3)	3.07×10^2 (3.02×10^2)	5.71×10^0 (5.7×10^0)	9.52×10^0 (9.62×10^0)
4	7.29×10^0 (6.71×10^0)	1.23×10^2 (1.23×10^2)	3.68×10^3 (3.56×10^3)	1.26×10^3 (1.2×10^3)	3.76×10^1 (3.89×10^1)	3.23×10^1 (3.12×10^1)
5	1.31×10^1 (1.13×10^1)	9.22×10^1 (9.2×10^1)	3.35×10^3 (3.29×10^3)	1.13×10^3 (1.09×10^3)	3.89×10^1 (4.06×10^1)	2.94×10^1 (2.87×10^1)
6	5.64×10^0 (5.03×10^0)	1.29×10^2 (1.28×10^2)	3.4×10^3 (3.34×10^3)	1.11×10^3 (1.09×10^3)	2.73×10^1 (2.83×10^1)	2.98×10^1 (2.92×10^1)
7	2.79×10^1 (2.78×10^1)	2.9×10^2 (2.83×10^2)	1.02×10^4 (1.01×10^4)	3.95×10^3 (3.86×10^3)	1.62×10^2 (1.64×10^2)	9.35×10^1 (9.2×10^1)
8	5.63×10^1 (4.94×10^1)	4.7×10^2 (4.56×10^2)	1.51×10^4 (1.49×10^4)	5.99×10^3 (5.94×10^3)	2.88×10^2 (2.93×10^2)	1.4×10^2 (1.39×10^2)
9	8.52×10^{-1} (8.06×10^{-1})	2.3×10^1 (2.25×10^1)	4.78×10^2 (4.88×10^2)	1.27×10^2 (1.36×10^2)	2.44×10^0 (2.49×10^0)	4×10^0 (4.11×10^0)
10	2.71×10^0 (2.43×10^0)	5.74×10^1 (5.7×10^1)	1.59×10^3 (1.58×10^3)	5.11×10^2 (5.22×10^2)	1.39×10^1 (1.47×10^1)	1.37×10^1 (1.37×10^1)
11	1.97×10^1 (1.98×10^1)	1.61×10^2 (1.58×10^2)	5.8×10^3 (5.74×10^3)	2.24×10^3 (2.19×10^3)	9.88×10^1 (1×10^2)	5.21×10^1 (5.15×10^1)
12	1.26×10^2 (1.3×10^2)	4.03×10^2 (3.94×10^2)	1.27×10^4 (1.25×10^4)	5.41×10^3 (5.31×10^3)	3.49×10^2 (3.5×10^2)	1.18×10^2 (1.16×10^2)
13	1.63×10^1 (1.53×10^1)	1.59×10^2 (1.56×10^2)	5.41×10^3 (5.27×10^3)	2.05×10^3 (1.97×10^3)	8.56×10^1 (8.71×10^1)	4.84×10^1 (4.71×10^1)
14	1.11×10^2 (1.16×10^2)	3.91×10^2 (3.62×10^2)	1.3×10^4 (1.27×10^4)	5.44×10^3 (5.31×10^3)	3.35×10^2 (3.37×10^2)	1.2×10^2 (1.18×10^2)

Table 7: Hot lines : all lines emission intensity ratios for the equilibrium ionization values in Tables 3 and 4, and Tables 5 and 6. The ratios calculated from the integrated intensity values are given in brackets.

#	94	131	193	211	335	TRACE 195
1	1.09×10^{-4} (1.44×10^{-3})	5.36×10^{-8} (1.12×10^{-8})	0.00 (0.00)	0.137 (0.102)	4.77×10^{-3} (0.111)	0.00 (0.00)
2	1.28×10^{-3} (2.66×10^{-3})	3.05×10^{-7} (3.56×10^{-8})	0.00 (0.00)	0.256 (0.135)	0.235 (0.146)	0.00 (0.00)
3	8.19×10^{-2} (2.42×10^{-2})	2.12×10^{-6} (4.19×10^{-7})	0.00 (0.00)	0.32 (0.232)	0.546 (0.359)	0.00 (0.00)
4	0.639 (0.321)	1.63×10^{-3} (1.42×10^{-4})	0.00 (0.00)	0.374 (0.289)	0.754 (0.638)	0.00 (0.00)
5	0.875 (0.657)	3.54×10^{-1} (9.92×10^{-4})	0.00 (0.00)	0.373 (0.287)	0.775 (0.686)	0.00 (0.00)
6	0.48 (0.158)	4.36×10^{-4} (1.06×10^{-4})	3.95×10^{-6} (5.8×10^{-7})	0.361 (0.269)	0.721 (0.549)	2.1×10^{-6} (3.16×10^{-7})
7	0.847 (0.556)	1.76×10^{-2} (1.82×10^{-3})	2.19×10^{-4} (1.38×10^{-5})	0.379 (0.294)	0.858 (0.741)	1.12×10^{-4} (7.14×10^{-6})
8	0.902 (0.679)	2.56×10^{-2} (2.8×10^{-3})	8.82×10^{-5} (8.49×10^{-5})	0.376 (0.29)	0.882 (0.774)	4.47×10^{-5} (4.36×10^{-5})
9	8.82×10^{-2} (2.19×10^{-2})	1.13×10^{-4} (1.21×10^{-5})	2.66×10^{-6} (6.32×10^{-7})	0.379 (0.257)	0.644 (0.378)	1.46×10^{-6} (3.61×10^{-7})
10	0.579 (0.159)	1.66×10^{-4} (7.38×10^{-5})	5.15×10^{-6} (8.37×10^{-7})	0.43 (0.307)	0.788 (0.6)	2.75×10^{-6} (4.64×10^{-7})
11	0.913 (0.64)	2.94×10^{-2} (2.02×10^{-3})	3.72×10^{-4} (2.62×10^{-5})	0.45 (0.328)	0.887 (0.763)	1.96×10^{-4} (1.38×10^{-5})
12	0.937 (0.857)	6.4×10^{-2} (2.14×10^{-2})	1.18×10^{-2} (9.38×10^{-4})	0.447 (0.329)	0.922 (0.837)	6.01×10^{-3} (4.82×10^{-4})
13	0.91 (0.585)	3.01×10^{-2} (1.2×10^{-3})	1.74×10^{-4} (4.82×10^{-5})	0.449 (0.323)	0.881 (0.746)	9.09×10^{-5} (2.57×10^{-5})
14	0.93 (0.848)	5.89×10^{-2} (1.47×10^{-2})	5.56×10^{-3} (5.93×10^{-4})	0.45 (0.324)	0.921 (0.83)	2.9×10^{-3} (3.04×10^{-4})

Table 8: Hot lines : all lines emission intensity ratios for the nonequilibrium ionization values in Tables 3 and 4, and Tables 5 and 6.

#	94	131	193	211	335	TRACE 195
1	0.00 (0.00)	0.00 (0.00)	0.00 (0.00)	0.00 (0.00)	0.00 (0.00)	0.00 (0.00)
2	0.00 (0.00)	0.00 (0.00)	0.00 (0.00)	0.224 (7.51×10^{-2})	0.00 (0.00)	0.00 (0.00)
3	0.00 (0.00)	0.00 (0.00)	0.00 (0.00)	0.338 (0.233)	0.611 (0.358)	0.00 (0.00)
4	0.636 (0.267)	0.00 (0.00)	0.00 (0.00)	0.38 (0.29)	0.794 (0.661)	0.00 (0.00)
5	0.886 (0.602)	0.00 (0.00)	0.00 (0.00)	0.376 (0.289)	0.806 (0.707)	0.00 (0.00)
6	0.474 (7.53×10^{-2})	0.00 (0.00)	0.00 (0.00)	0.367 (0.271)	0.743 (0.572)	0.00 (0.00)
7	0.872 (0.565)	1.52×10^{-2} (4.92×10^{-4})	0.00 (0.00)	0.377 (0.293)	0.865 (0.75)	0.00 (0.00)
8	0.921 (0.642)	1.97×10^{-2} (6.1×10^{-4})	0.00 (0.00)	0.381 (0.29)	0.887 (0.782)	0.00 (0.00)
9	0.00 (0.00)	0.00 (0.00)	0.00 (0.00)	0.423 (0.274)	0.668 (0.365)	0.00 (0.00)
10	0.589 (8.15×10^{-2})	0.00 (0.00)	0.00 (0.00)	0.44 (0.316)	0.812 (0.614)	0.00 (0.00)
11	0.932 (0.646)	2.26×10^{-2} (5.74×10^{-4})	0.00 (0.00)	0.445 (0.325)	0.902 (0.77)	0.00 (0.00)
12	0.934 (0.862)	4.64×10^{-2} (1.74×10^{-2})	0.00 (0.00)	0.441 (0.328)	0.928 (0.84)	0.00 (0.00)
13	0.923 (0.566)	2.26×10^{-2} (2.85×10^{-4})	0.00 (0.00)	0.449 (0.322)	0.888 (0.758)	0.00 (0.00)
14	0.931 (0.858)	5.23×10^{-2} (9.93×10^{-3})	0.00 (0.00)	0.446 (0.32)	0.927 (0.834)	0.00 (0.00)

Table 9: Intensities (DN pixel⁻¹ s⁻¹) at the loop apex for a selection of Hinode-EIS emission lines. Values calculated for nonequilibrium ionization are given in brackets for each run.

#	Fe XI	XII	XV	XVI	XVII	Ca XVII
1	1.23×10^{-2} (1.48×10^{-2})	1.06×10^{-1} (1.12×10^{-1})	1.14×10^{-3} (0.00)	2.55×10^{-6} (0.00)	6.71×10^{-9} (0.00)	1.48×10^{-7} (0.00)
2	3.4×10^{-2} (3.73×10^{-2})	3.22×10^{-1} (3.86×10^{-1})	2.4×10^{-2} (1.29×10^{-2})	5.65×10^{-4} (0.00)	9.54×10^{-7} (0.00)	4.43×10^{-6} (0.00)
3	1.11×10^{-1} (1.03×10^{-1})	1.38×10^0 (1.28×10^0)	1.96×10^{-1} (2.34×10^{-1})	9.89×10^{-3} (1.25×10^{-2})	1.21×10^{-4} (9.58×10^{-5})	3.45×10^{-4} (0.00)
4	2.33×10^{-1} (2.12×10^{-1})	3.21×10^0 (2.78×10^0)	9.64×10^{-1} (9.88×10^{-1})	7.21×10^{-2} (8.06×10^{-2})	2.1×10^{-3} (2.3×10^{-3})	2.66×10^{-2} (1.35×10^{-2})
5	2.01×10^{-1} (1.85×10^{-1})	2.81×10^0 (2.57×10^0)	7.64×10^{-1} (7.78×10^{-1})	6.47×10^{-2} (7.25×10^{-2})	4.35×10^{-3} (4.97×10^{-3})	8.79×10^{-2} (9.63×10^{-2})
6	2.7×10^{-1} (2.54×10^{-1})	3.69×10^0 (3.51×10^0)	1.03×10^0 (1.05×10^0)	7.09×10^{-2} (7.59×10^{-2})	1.79×10^{-3} (1.83×10^{-3})	1.85×10^{-2} (8.23×10^{-3})
7	4.66×10^{-1} (4.44×10^{-1})	6.94×10^0 (6.53×10^0)	3.48×10^0 (3.4×10^0)	3.66×10^{-1} (3.71×10^{-1})	1.39×10^{-2} (1.44×10^{-2})	1.73×10^{-1} (2.83×10^{-1})
8	5.55×10^{-1} (5.29×10^{-1})	8.32×10^0 (7.88×10^0)	4.61×10^0 (4.58×10^0)	5.59×10^{-1} (5.68×10^{-1})	2.81×10^{-2} (2.93×10^{-2})	4.02×10^{-1} (5.35×10^{-1})
9	1.16×10^{-2} (9.72×10^{-3})	1.49×10^{-1} (1.36×10^{-1})	2.62×10^{-2} (3.39×10^{-2})	1.49×10^{-3} (1.74×10^{-3})	1.55×10^{-5} (1.08×10^{-5})	9.8×10^{-6} (0.00)
10	2.29×10^{-2} (2.05×10^{-2})	3.32×10^{-1} (2.95×10^{-1})	1.07×10^{-1} (1.1×10^{-1})	8.67×10^{-3} (9.35×10^{-3})	2.18×10^{-4} (2.21×10^{-4})	1.92×10^{-3} (0.00)
11	4.99×10^{-2} (4.55×10^{-2})	7.8×10^{-1} (6.88×10^{-1})	4.36×10^{-1} (4.14×10^{-1})	5.24×10^{-2} (5.35×10^{-2})	2.66×10^{-3} (2.8×10^{-3})	4×10^{-2} (5.12×10^{-2})
12	8.17×10^{-2} (7.47×10^{-2})	1.36×10^0 (1.24×10^0)	1.01×10^0 (9.65×10^{-1})	1.59×10^{-1} (1.59×10^{-1})	1.25×10^{-2} (1.25×10^{-2})	2.24×10^{-1} (2.25×10^{-1})
13	5.06×10^{-2} (4.67×10^{-2})	8.02×10^{-1} (7.16×10^{-1})	4.23×10^{-1} (4.12×10^{-1})	4.89×10^{-2} (5.04×10^{-2})	2.52×10^{-3} (2.65×10^{-3})	3.83×10^{-2} (4.91×10^{-2})
14	9×10^{-2} (8.48×10^{-2})	1.33×10^0 (1.23×10^0)	1.02×10^0 (9.81×10^{-1})	1.57×10^{-1} (1.57×10^{-1})	1.22×10^{-2} (1.24×10^{-2})	2.17×10^{-1} (2.29×10^{-1})

Table 10: Integrated intensities (DN s^{-1}) along the loop for a selection of Hinode-EIS emission lines.

#	Fe XI	XII	XV	XVI	XVII	Ca XVII
1	3.88×10^{-1} (3.31×10^{-1})	2.52×10^0 (1.55×10^0)	9.9×10^{-2} (0.00)	3.71×10^{-3} (0.00)	2.33×10^{-5} (0.00)	1.67×10^{-5} (0.00)
2	1.25×10^0 (1.42×10^0)	9.19×10^0 (9.94×10^0)	4.15×10^{-1} (5.98×10^{-2})	1.37×10^{-2} (0.00)	8.46×10^{-5} (0.00)	2.12×10^{-4} (0.00)
3	6.92×10^0 (7.07×10^0)	7.03×10^1 (7.18×10^1)	6.32×10^0 (6.54×10^0)	2.68×10^{-1} (2.63×10^{-1})	2.66×10^{-3} (1.35×10^{-3})	9.63×10^{-8} (0.00)
4	2.04×10^1 (2×10^1)	2.39×10^2 (2.3×10^2)	4.9×10^1 (5.01×10^1)	3.22×10^0 (3.44×10^0)	7.19×10^{-2} (7.51×10^{-2})	7.6×10^{-1} (2.39×10^{-1})
5	1.91×10^1 (1.89×10^1)	2.22×10^2 (2.16×10^2)	4.44×10^1 (4.57×10^1)	3.65×10^0 (3.91×10^0)	1.81×10^{-1} (1.95×10^{-1})	3.2×10^0 (1.45×10^0)
6	1.89×10^1 (1.86×10^1)	2.15×10^2 (2.1×10^2)	3.61×10^1 (3.73×10^1)	1.99×10^0 (2.14×10^0)	3.27×10^{-2} (3.32×10^{-2})	2.6×10^{-1} (2.86×10^{-2})
7	5.14×10^1 (5.08×10^1)	6.36×10^2 (6.23×10^2)	2.03×10^2 (2.03×10^2)	1.63×10^1 (1.66×10^1)	4.28×10^{-1} (4.53×10^{-1})	4.44×10^0 (5.87×10^0)
8	7.22×10^1 (7.17×10^1)	8.92×10^2 (8.78×10^2)	3.35×10^2 (3.41×10^2)	3.04×10^1 (3.13×10^1)	9.94×10^{-1} (1.1×10^0)	1.17×10^1 (1.14×10^1)
9	3.05×10^0 (3.05×10^0)	3.09×10^1 (3.19×10^1)	2.85×10^0 (3.47×10^0)	1.2×10^{-1} (1.17×10^{-1})	1.05×10^{-3} (3.51×10^{-4})	3.72×10^{-3} (0.00)
10	9.27×10^0 (9.18×10^0)	1.07×10^2 (1.07×10^2)	1.85×10^1 (2.03×10^1)	1.11×10^0 (1.21×10^0)	1.78×10^{-2} (1.39×10^{-2})	1.14×10^{-1} (0.00)
11	3.03×10^1 (3×10^1)	3.87×10^2 (3.81×10^2)	1.2×10^2 (1.2×10^2)	1.03×10^1 (1.05×10^1)	3.33×10^{-1} (3.39×10^{-1})	4.07×10^0 (4.67×10^0)
12	6.16×10^1 (6.09×10^1)	8.09×10^2 (7.96×10^2)	3.67×10^2 (3.65×10^2)	4.03×10^1 (4.06×10^1)	2.08×10^0 (2.11×10^0)	3.27×10^1 (3.4×10^1)
13	2.86×10^1 (2.8×10^1)	3.58×10^2 (3.46×10^2)	1.05×10^2 (1.05×10^2)	8.69×10^0 (8.96×10^0)	2.65×10^{-1} (2.84×10^{-1})	3.1×10^0 (3.02×10^0)
14	6.31×10^1 (6.22×10^1)	8.16×10^2 (7.96×10^2)	3.57×10^2 (3.55×10^2)	3.82×10^1 (3.87×10^1)	1.88×10^0 (1.99×10^0)	2.89×10^1 (3.05×10^1)

Table 11: Nonequilibrium : equilibrium intensity ratios for the values in Tables 9 and 10. The ratios calculated from the integrated intensity values are given in brackets.

#	Fe XI	XII	XV	XVI	XVII	Ca XVII
1	1.2 (0.85)	1.06 (0.62)	0.00 (0.00)	0.00 (0.00)	0.00 (0.00)	0.00 (0.00)
2	1.1 (1.14)	1.2 (1.08)	0.54 (0.14)	0.00 (0.00)	0.00 (0.00)	0.00 (0.00)
3	0.93 (1.02)	0.93 (1.02)	1.19 (1.03)	1.26 (0.98)	0.79 (0.51)	0.00 (0.00)
4	0.91 (0.98)	0.87 (0.96)	1.02 (1.02)	1.12 (1.07)	1.1 (1.04)	0.51 (0.31)
5	0.92 (0.99)	0.92 (0.97)	1.02 (1.03)	1.12 (1.07)	1.14 (1.08)	1.1 (0.45)
6	0.94 (0.98)	0.95 (0.98)	1.02 (1.03)	1.07 (1.08)	1.02 (1.02)	0.45 (0.11)
7	0.95 (0.99)	0.94 (0.98)	0.98 (1)	1.01 (1.02)	1.04 (1.06)	1.64 (1.32)
8	0.95 (0.99)	0.95 (0.98)	0.99 (1.02)	1.02 (1.03)	1.04 (1.11)	1.33 (0.97)
9	0.84 (1)	0.91 (1.03)	1.29 (1.22)	1.17 (0.98)	0.7 (0.33)	0.00 (0.00)
10	0.9 (0.99)	0.89 (1)	1.03 (1.1)	1.08 (1.09)	1.01 (0.78)	0.00 (0.00)
11	0.91 (0.99)	0.88 (0.98)	0.95 (1)	1.02 (1.02)	1.05 (1.02)	1.28 (1.15)
12	0.91 (0.99)	0.91 (0.98)	0.96 (0.99)	1 (1.01)	1 (1.01)	1 (1.04)
13	0.92 (0.98)	0.89 (0.97)	0.97 (1)	1.03 (1.03)	1.05 (1.07)	1.28 (0.97)
14	0.94 (0.99)	0.92 (0.98)	0.96 (0.99)	1 (1.01)	1.02 (1.06)	1.06 (1.06)

REFERENCES

- Aschwanden, M. J., Nightingale, R. W. & Alexander, D., 2000, *ApJ*, 541, 1059
- Bradshaw, S. J., 2009, *A&A*, 502, 409
- Bradshaw, S. J. & Cargill, P. J., 2005, *A&A*, 437, 311
- Bradshaw, S. J. & Cargill, P. J., 2006, *A&A*, 458, 987
- Bradshaw, S. J. & Cargill, P. J., 2010, *ApJ*, 717, 163
- Cargill, P. J., 1994, *ApJ*, 422, 381
- Cargill, P. J., & Klimchuk, J. A., 1997, *ApJ*, 478, 799
- De Pontieu, B., McIntosh, S. W., Hansteen, V. H. & Schrijver, C. J., 2009, *ApJ*, 701, L1
- Dere, K. P., Landi, E., Mason, H. E., Monsignori Fossi, B. C. & Young, P. R.,
1997, *A&AS*, 125, 149
- Golub, L., Hartquist, T. W., Quillen, A. C., 1989, *Sol. Phys.*, 122, 245
- Hara, H., Watanabe, T., Harra, L. K., Culhane, J. L., Young, P. R., Mariska, J. T. & Doschek, G. A.,
2008, *ApJ*, 678, L67
- Klimchuk, J. A., 2006, *Sol. Phys.*, 234, 41
- Klimchuk, J. A., 2009, in *The Second Hinode Science Meeting: Beyond Discovery—Toward Understanding* (ASP Conf. Ser. Vol. 415), ed. B. Lites et al. (San Francisco: Astron. Soc. Pacific), 221
- Klimchuk, J. A., Karpen, J. T. & Antiochos, S. K., 2010, *ApJ*, 714, 1239

- Landi, E., Del Zanna, G., Young, P. R., Dere, K. P., Mason, H. E. & Landini, M.,
2006, *ApJS*, 162, 261
- Longcope, D. W. & Bradshaw, S. J., 2010, *ApJ*, 718, 1491
- McTiernan, J. M., 2009, *ApJ*, 697, 94
- O’Dwyer, B. O., Del Zanna, G., Mason, H. E., Sterling, A. C., Tripathi, D. & Young, P. R.,
2010, *A&A*, 2010.
- Parker, E. N., 1988, *ApJ*, 330, 474
- Patsourakos, S. & Klimchuk, J. A., 2006, *ApJ*, 647, 1452
- Patsourakos, S., Klimchuk, J. A. & MacNeice, P. J., 2004, *ApJ*, 603, 322
- Porter, L. J. & Klimchuk, J. A., 1995, *ApJ*, 454, 499
- Reale, F., Testa, P., Klimchuk, J. A. & Parenti, S., 2009a, *ApJ*, 698, 756
- Reale, F., McTiernan, J. M. & Testa, P., 2009b *ApJ*, 704, L58
- Reale, F. & Orlando, S., 2008, *ApJ*, 684, 715
- Reale, F. & Peres, G., 2000, *ApJ*, 528, L45
- Schmelz, J. T. Saar, S. H., DeLuca, E. E., Golub, L., Kashyap, V. L., Weber, M. A. &
Klimchuk, J. A., 2009a, *ApJ*, 693, L131
- Schmelz, J. T., Kashyap, V. L., Saar, S. H., Dennis, B. R., Grigis, P. C., Lin, L., De Luca, E. E.,
Holman, G. D., Golub, L. & Weber, M. A., 2009b, *ApJ*, 704, 863
- Spadaro, D., Lanza, A. F., Lanzafame, A. C., Karpen, J. T., Antiochos, S. K., Klimchuk, J. A. &
MacNeice, P. J., 2003, *ApJ*, 582, 486

Sylwester, B., Sylwester, J. & Phillips, K. J. H., 2010, A&A, 514, 82

Warren, H. P., Winebarger, A. R. & Brooks, D. H., 2010, ApJ, 711, 228

Warren, H. P., Winebarger, A. R. & Hamilton, P. S., 2002, ApJ, 579, L41

Winebarger, A. R., Warren, H. P., van Ballegooijen, A., DeLuca, E. E., & Golub, L.,
2002, ApJ, 567, L89